We are IntechOpen, the world's leading publisher of Open Access books Built by scientists, for scientists

6,900
Open access books available

185,000
International authors and editors

200M
Downloads

154
Countries delivered to

Our authors are among the

TOP 1%
most cited scientists

12.2%
Contributors from top 500 universities

CLARIVATE ANALYTICS
BOOK CITATION INDEX
INDEXED

WEB OF SCIENCE™

Selection of our books indexed in the Book Citation Index
in Web of Science™ Core Collection (BKCI)

Interested in publishing with us?
Contact book.department@intechopen.com

Application of RP and Manufacturing to Water-Saving Emitters

Zhengying Wei
Xi'an Jiaotong University
China

1. Introduction

1.1 Introduction of water-saving drip irrigation emitters

In order to solve the problem of water shortage in agriculture, it's necessary to develop water-saving irrigation (Bralts & Vincent, 1985). At present, there are more than ten kinds of water-saving irrigation models including the anti-seepage of channels, low pressure irrigation, sprinkler irrigation, micro irrigation, under-membrane irrigation, over-membrane irrigation. Among these irrigation patterns, drip irrigation is the most effective way in arid and semi-arid areas and its utilization rate can reach up to 90% (Thompson et al., 2009; Lamm F. R. & Camp C. R., 2007; Onder et al., 2005; Schwankl & Hanson, 2007; Cetin & Bilgel, 2002).

Drip irrigation is such an irrigation method that transfers the water under a definite pressure, after filtering, through pipe network into the soil surrounding the root system of plants in drops slowly and uniformly. As the key device in drip irrigation systems, the emitter is to drip the pressured water in the pipeline to the root of the crops evenly and steadily, so as to guarantee the water demand for crop growth. The quality of the emitter has an important effect on the reliability, life span of the drip irrigation system and irrigation quality (Schwankl & Hanson, 2007).

1.2 Structure design and flow rate prediction of micro channel emitter

Usually, the structure of the emitter channel is very complex with a dimension of 0.8mm-1.2mm (Wei et al., 2007). Emitter's intricate inner channel makes the flow of water have turbulent behavior. As a result, the behavior index will be decreased and the flow rate will be insensitive to the pressure. With all the above advantages, an evened uniform guaranteed irrigation will be improved. So, in the process of design, the channel length will be decreased and the manufacturing cost of the emitter will be reduced. It is the common goal of emitter designer to decrease the flow state index on the basis of simplifying the emitter structure (Li et al., 2005).

In the design of emitter structure, we use 3D parametric CAD software PRO/E to design labyrinth emitter. Fig. 1. shows 4 typical labyrinth channels with their crucial dimensions. According to emitter's hydraulic performance and its requirement for anti-clogging, we can design new channel structures by changing those dimensions.

The irrigation quality of drip irrigation system is verified by emitter's hydraulic performance (Li et al., 2008). In the high-pressure pipeline, the water energy may dissipate

after flowing through the labyrinth channel and the flow rate can be controlled to meet the water need of the crops. To ensure the emitter's hydraulic performance, before the fabrication of emitter, computational fluid dynamics (CFD) is used to predict emitter's flow rate and analyze its hydraulic performance under various water pressures. If the structure can meet the water flow's requirement very well, then rapid prototyping (RP) is conducted to fabricate the emitter, and also related experiments are performed to test the performance. The simulation process using CFD to predict flow rate is shown in Fig. 2.

Fig. 1. Structure of four typical labyrinth channel

Fig. 2. Flow rate prediction with the use of CFD

1.3 Integrating RP manufacture of emitter

Currently, the traditional method is used in emitter development, the steps are shown in Fig. 3. The period of emitter development is generally 4 to 5 months, leading to high cost and low accuracy. However, taking RP&M technique into the emitter development can solve these problems conveniently.
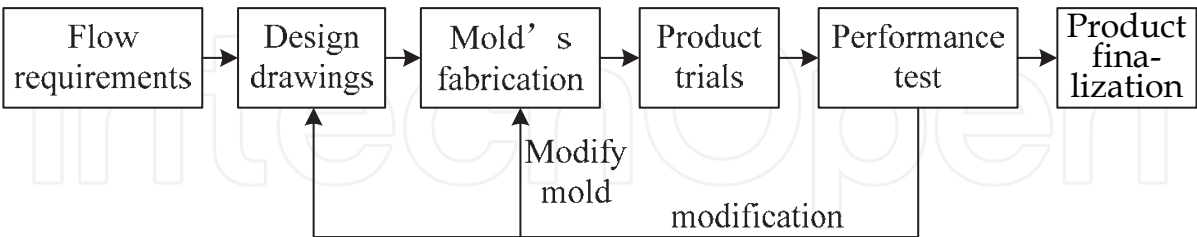
Fig. 3. Development steps of emitter product

The emitter's rapid development process based on RP&M is shown in Fig. 4. Taking fluid dynamics and integration of RP technique as the core, the closed-loop control of the product development is exercised, and the design and development cycle are greatly reduced, which provide a platform for emitter's design and verification. Finaly the design efficiency is greatly improved (Wei et al., 2007).
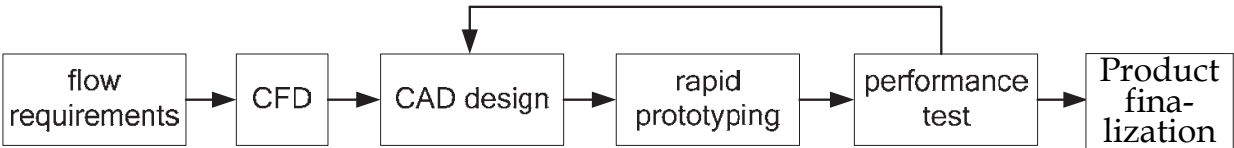
Fig. 4. Rapid development processes of emitter (Wei et al., 2003)

The emitter's performance is directly affected by the structure of the labyrinth channel (Wei & Lu, 2005). The more complex the channel boundary is, the smaller the flow state index will be. In order to achieve a low flow rate and control the emitter's flow rate, the viscous resistance of channel to water should be large enough to reduce the water flow rate under a certain pressure. The main factors influencing the channel viscous resistance include the cross-section shape, length and shape of channel. Besides, the channel should be smooth and the mold's fabrication should be considered when designing the emitter. The sharp structure and sudden turning in the connection area of channels should be eliminated to avoid vortexes and stagnation area which will cause particle deposition and microorganism growth and eventually the emitter clogging (Wei et al., 2008).

The length, width and height of the emitter channel are taken as the design parameters and hence a parametric design scheme is formed. Emitter's model is shown in Fig. 5.
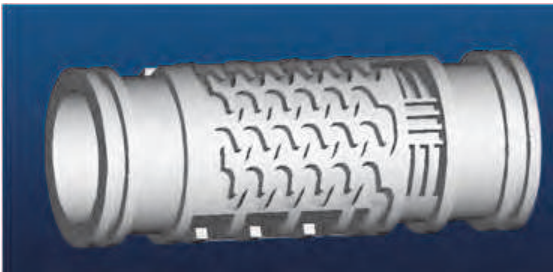
Fig. 5. Emitter's CAD model

The emitter and the outer tube are designed as a whole by adding an outer tube encapsulating the emitter directly. The integration of 3D CAD model is shown in Fig. 6.
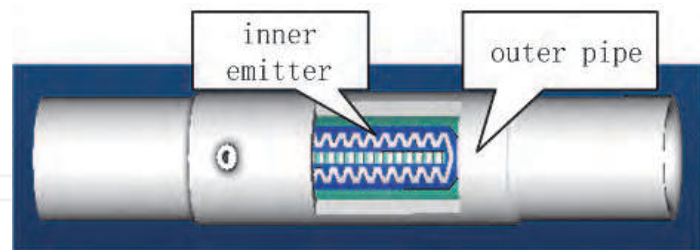

Fig. 6. Integration of experimental three-dimensional solid CAD model of emitter

To finalize the dimensions of the designed emitter as soon as possible, rapid prototyping and manufacturing (RP&M) is used to develop the emitter. The experimental prototype of the emitter is fabricated. It can be directly used in pressure flow experiments.

2. Emitter's rapid prototyping manufacturing technology

RP of emitter is the key stage in emitter's rapid development. The following contents will introduce the emitter's RP fabricating in detail.

2.1 Introduction of rapid prototyping

Rapid Prototyping is a new advanced manufacturing technology developed in early 1980's. The core idea of this technology is based on dimension reduction discrete methods (White, 2001). A complex three-dimensional object is firstly sliced, and then converted into two-dimensional planes. The RP machine builds the object layer by layer and finally fabricates the part (Hosni & Sundaram, 1996).

According to various materials used in RP manufacturing, the RP process can be classified as shown in Fig. 7 (Yan & Gu, 1996).
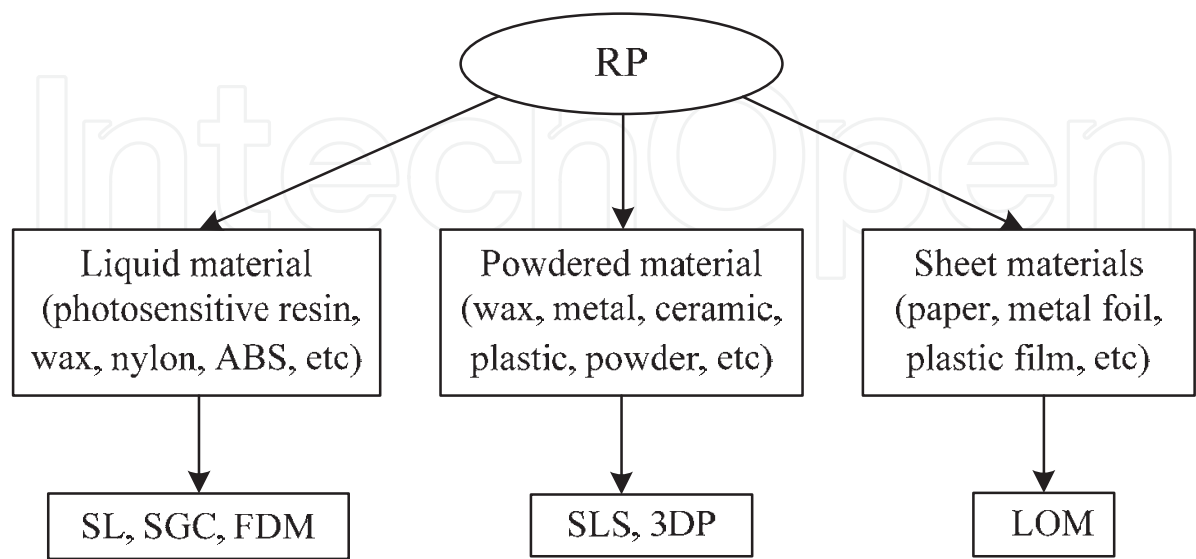

Fig. 7. Classification of RP process

The products fabricated by SL process have the advantages of better surface quality and higher accuracy (about 0.05mm) and the SL process has higher system resolution (Pham & Gault, 1998). This method has been widely used in the manufacturing field (White, 2001).

2.2 Rapid prototyping and fabrication of emitter's integrated model

SL process can be divided into the following steps: using software to construct three-dimensional model or using reverse technology to obtain product's entity (physical models) directly (Choi & Samavedam, 2002), and then transferring the model's data into STL file, using slicing software to slice the model with the required accuracy, getting a set of contour-parallel offset data, and then using software to add support for the contour-parallel offset data. The main purpose of adding support is to facilitate the forming of cavity and suspension, and it can reduce the deformation. The laser is used under the control of scanning system. A thin solidified layer is formed on the photosensitive resin, then the platform sinks until the distance between solidified layer and the resin surface is the thickness of a layer (0.05mm), repeat the process, eventually a solid prototype is formed. Fig. 8 is the scheme of emitter's forming process. STL data is the interface of CAD / RP data which is composed of a large number of triangular facets approximating the part's shape. The more the facets are, the higher the accuracy of approximation will be.
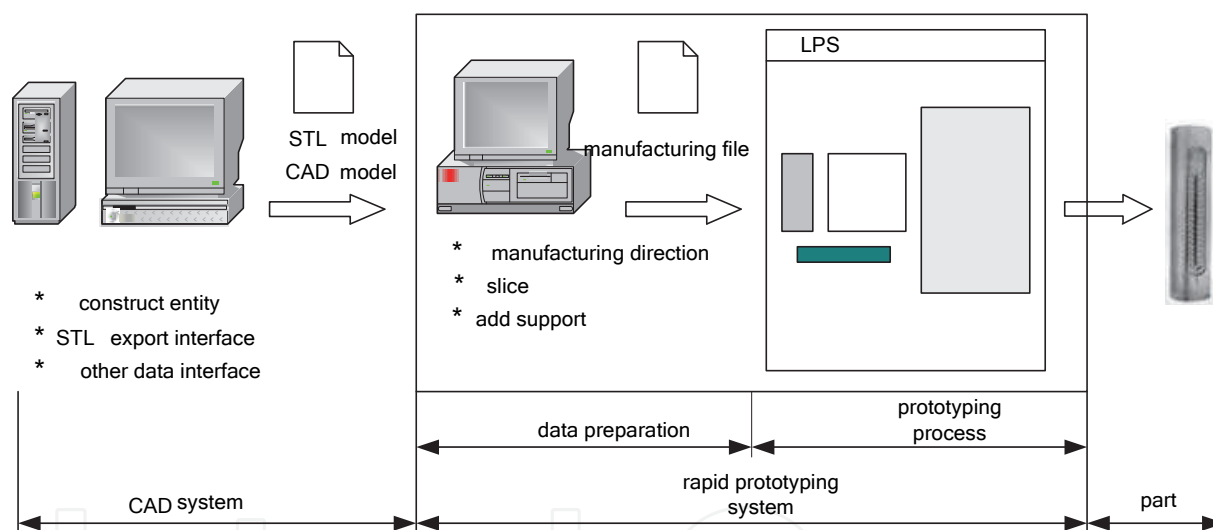

Fig. 8. Scheme of rapid prototyping process

The fabrication process of emitter and its integrating prototyping are as follows, Pro/E is firstly used to design the parameters of emitter and establish the three-dimensional CAD model (as Figure 1-5 and Figure 1-6); then the model is converted into STL files and slicing software is used to cut the model, the cuts can be fabricated in a rapid prototyping machine after adding support. The schematic diagram of detailed production process schematic diagram is shown in Fig. 9 (Wei et al., 2008). The integrating of irrigation emitter and its experimental prototype are shown in Fig. 10.

2.3 Accuracy analysis and compensation of emitter prototypes

The emitter prototypes are manufactured by SPS-350B rapid prototyping machine. When using this machine, there are many empirical parameters such as laser sweeping power: 280MW; solidified layer thickness: 0.1mm; the laser spot size: 0.12mm; power output of

post-curing box: 40W, temperature of post-curing box: 20°C; sweeping mode: XYSTA, (interlacing sweeping). The deviations in X and Y directions are similar.

Emitter channel is built in horizontal direction. Experimental results show that the deviation in this direction is very small ranging from zero to 5 percent. While in the X-Y plane the accuracy is poor, so the accuracy in X-Y plane is discussed.
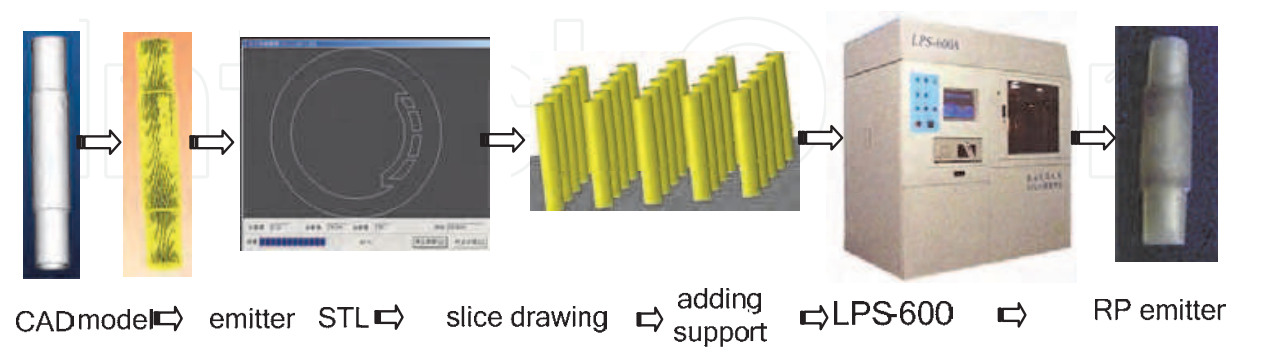

CAD model ⇨ emitter STL ⇨ slice drawing ⇨ adding support ⇨ LPS-600 ⇨ RP emitter

Fig. 9. Manufacture process of integrated emitter prototype

(a) emitter's prototype   (c) emitter's integrated experimental prototype

(b) sheet-dropper's prototype   (d) sheet-dropper's integrated experimental prototype
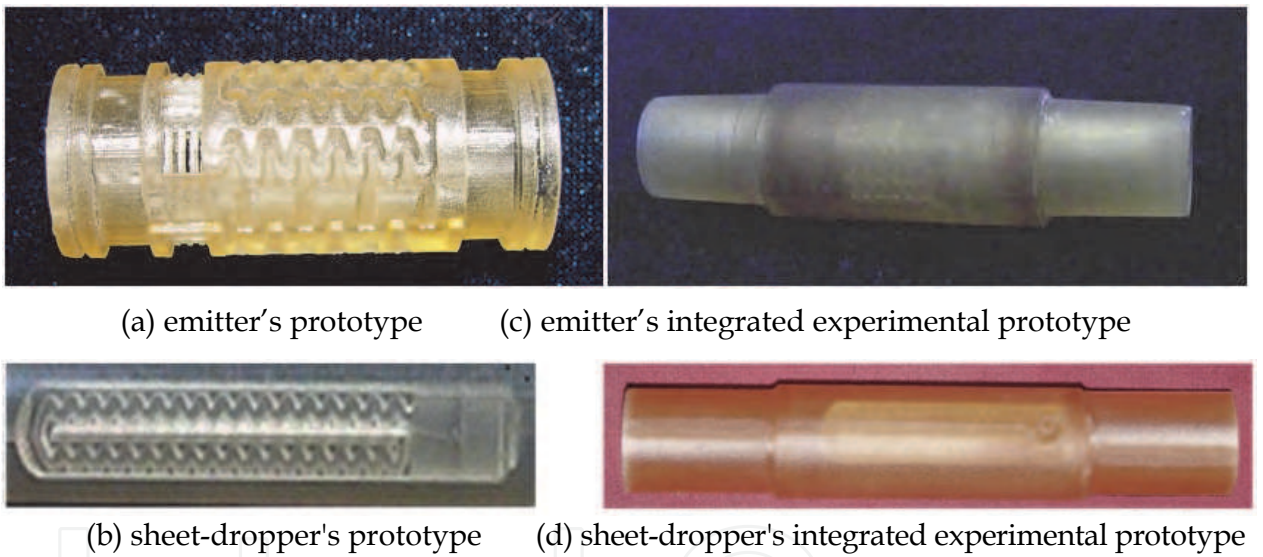
Fig. 10. Experimental prototype and integration of emitter

2.3.1 Derivation of crucial parameters

Some parallel grooves on the plate are built to measure X and Y directions' deviation by measuring groove width and the ridge width (the spacing between grooves). The rapid prototyped parts are shown in Fig. 11(a). The size parameters are as follow: groove width: 1mm; ridge width: 1mm; groove depth: 1mm; sample length: 30mm; sample width: 10mm; sample thickness: 2mm.

The process parameters of rapid prototypes are as follows: laser sweeping power: 280MW; layer thickness: 0.1mm; compensation dimension: 0.12mm; sweeping mode: XYSTA; power output of post-curing box: 40W. According to the actual operation situation of RP machine, the approximate processing parameters are determined: sweeping speed: 2000mm/s~8000mm/s; post-curing time: 10min~35min. During the experiment, the speed are divided into 7 levels: 2000mm/s, 3000mm/s, 4000mm/s, 5000mm/s, 6000mm/s,

7000mm/s, 8000mm/s; and the post-curing time is divided into 6 levels: 10min, 15min, 20min, 25min, 30min, 35min. These different levels are combined to make different testing samples, and the samples are measured to get the accuracy deviation of the parts.

Compensation is made for arc experimental samples. As Fig. 11(b) shows, in order to distinguish from other samples, single side fillets are designed in the experimental sample. The unit width of the experimental sample is 3mm, the angle of sharp corner is 60°, a channel is composed of 10 units, the depth of channel is 0.5mm, the radius of fillet are from 0.1mm to 0.5mm with an interval of 0.05mm, the fillets radius of sharp corner and groove are measured to determine the compensation value in both cases.
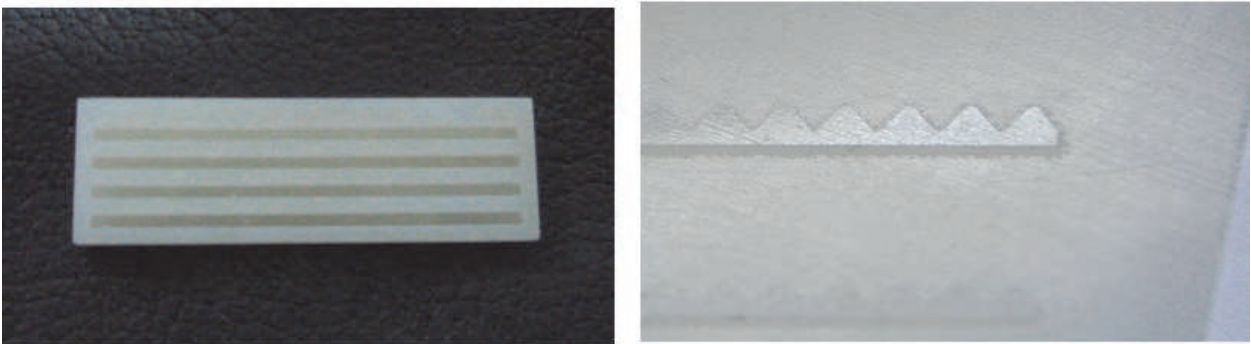
Fig. 11. Rapid prototyped experimental samples
(a) X and Y directions deviation testing sample (b) Circular arc compensation testing sample

2.3.2 Experimental results and accuracy analysis of RP parts

Microscope system VH-8000 is used for detecting the building accuracy of the experimental samples.

(1) Measurement errors in X and Y directions

The measurement errors in X and Y directions are shown in Table 1 and 2.

scanning velocity (mm/s) Post-cured time/(min)	2000	3000	4000	5000	6000	7000	8000
10	11.76	5.29	4.90	3.14	2.16	2.55	3.53
15	9.81	4.30	2.65	4.51	2.84	5.39	7.89
20	6.97	3.93	2.16	3.43	2.35	0.59	7.26
25	6.37	3.83	2.35	3.14	0.98	0.68	2.16
30	6.28	3.73	1.18	5.88	4.61	1.18	5.20
35	5.49	3.04	2.55	2.55	2.45	0.10	3.24

Table 1. Measurement errors of ridge width under different experimental conditions(%)

scanning velocity (mm/s) Post-cured time/(min)	2000	3000	4000	5000	6000	7000	8000
10	-12.74	-6.76	-7.45	-5.49	-4.61	-3.53	-5.19
15	-10.19	-5.68	-5.98	-5.2	-3.04	-8.23	-8.42
20	-8.43	-5.35	-4.12	-6.36	-3.43	-3.04	-6.86
25	-8.24	-4.9	-4.21	-3.92	-5.19	-3.72	-3.93
30	-6.96	-4.8	-1.49	-5.1	-4.71	-1.86	-7.06
35	-6.86	-3.82	-5.19	-5	-4.21	-2.73	-3.33

Table 2. Measurement errors of groove width under different experimental conditions(%)

Analysis of experimental results: The results are shown by the error curve changes with the parameters.
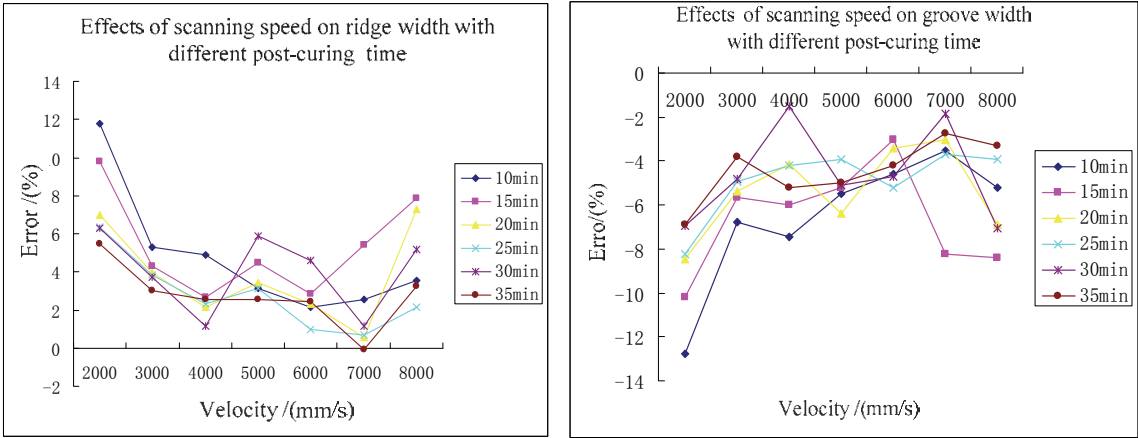
(a) Effects of scanning speed on ridge width (b) Effects of scanning speed on groove width

Fig. 12. The curves indicate the effect of scanning speed and post-curing times on error
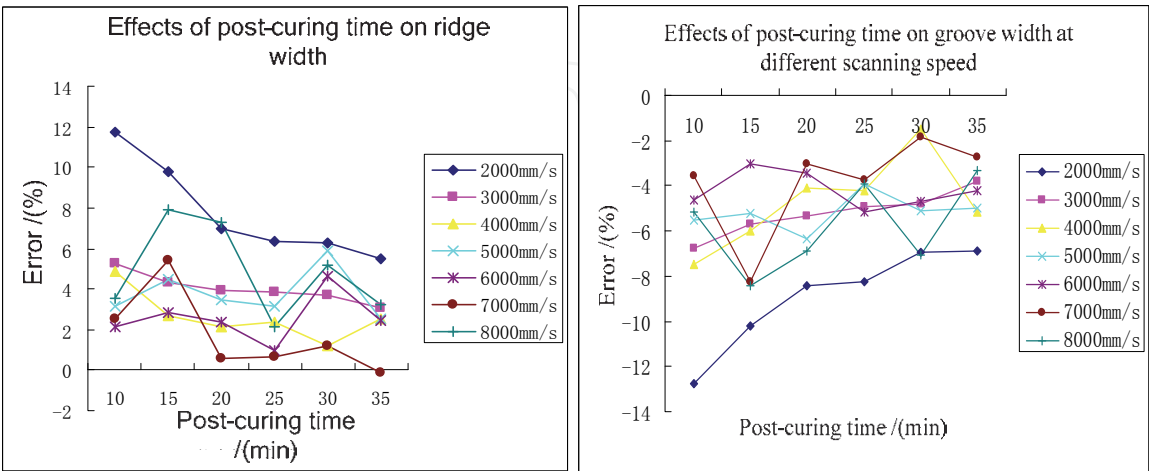
(a) Effects of post-curing time on ridge width (b) Effects of post-curing time on groove width

Fig. 13. The curves indicate the effect of post-curing times and scanning speed on error

The figures show that the error, at the same scanning speed, is reduced as the post-curing time prolonging and the error changes little after 25min post-curing. From the curves of 8 different scanning speeds, we can conclude that after post-curing for 25min, the error can be ignored.

It was found that the error of ridge width is generally positive while the error of groove width is negative. However, the summation of two is not exactly equal to 2mm. Under different process conditions, the width errors of the two units are measured to determine the final building parameters.

Table 3 shows that the best experimental result is achieved with a scanning speed of 6000mm/s and post-curing time of 30min. The overall error is 0.05% under this process condition. The error of groove width is 4.71% and the error of ridge width is 4.61%, both are less than 5%, meeting the design requirements.

scanning velocity/ (mm/s) Post-cured time/(min)	2000	3000	4000	5000	6000	7000	8000
10	-0.535	-0.49	-1.275	-1.175	-1.225	-0.49	-0.83
15	-0.73	-0.19	-1.665	-0.345	-0.1	-1.42	-0.265
20	-0.525	-0.635	-0.98	-1.465	-0.54	-1.225	0.2
25	-0.935	-0.975	-0.93	-0.39	-2.105	-1.52	-0.885
30	-0.34	-0.435	-0.155	0.39	-0.05	-0.34	-0.93
35	-0.785	-0.39	-1.32	-1.225	-0.88	-1.415	-0.045

Table 3. Total measuring error under various experimental conditions(%)

(2)Accuracy measurement of experimental samples for arc compensation
The measurement results of experimental samples for arc compensation are shown in Table 4.

theoretical dimension/(mm)	sharp corner/(mm)	groove/(mm)
0.1	0.096	0.106
0.15	0.138	0.167
0.2	0.178	0.218
0.25	0.233	0.264
0.3	0.278	0.310
0.35	0.325	0.355
0.4	0.365	0.408
0.45	0.429	0.453
0.5	0.485	0.501

Table 4. The results of arc compensation obtained from experiments

From the table, we can get the curve of experimental samples for arc compensation, shown in Fig. 14.

From this curve, the designed values required by actual dimension are obtained. When the radius are ranged from 0.1mm to 0.5mm, the dimensions of experimental samples can get proper compensation. The range of radius in the table can be expanded if needed.
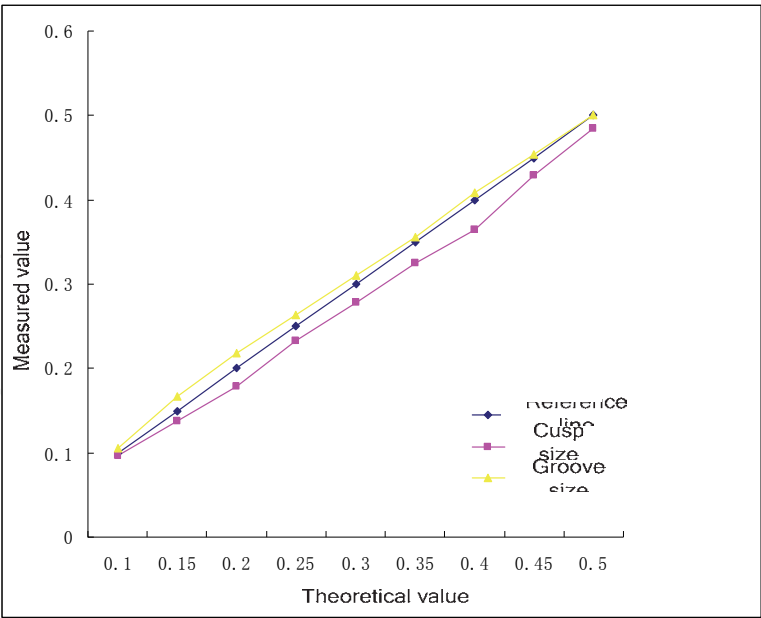
Fig. 14. The curve of experimental samples for arc compensation

The figure shows that the error of groove is obviously less than sharp corner. This is because the contraction of the substrate may affect the actual size of groove and the local contraction of sharp corner may affect the actual size of sharp corner. However, the larger the substrate, the less obvious the contraction. As the size of the substrate increases, the errors of groove and sharp corner first increase and then decrease. When the fillet radius of the groove is larger than 0.35mm, the dimension of exprimental sample is consistent with the designed value except a very small error.

3. Analyzing of anti-clogging mechanism and rapid experimental research based on PIV

The hydraulic behavior and anti-clogging performance are the two key indexes of the emitter (Zhang et al., 2009; Liu et al.,2010; Li et al., 2006; Zhang et al., 2007; Meng et al., 2004; Wei Z. et al., 2008; Wei Q. et al., 2006). In order to analyze the hydraulic behavior and anti-clogging performance of these emitters in actual use, rapid prototyping was used to fabricate the experimental samples. Then the visualized experiments with the use of PIV and CFD-based numerical computation were conducted to perform the analysis of the hydraulic behavior and anti-clogging performance. The structural parameters of the emitter were then analyzed and the structure of the labyrinth channel was optimized.

3.1 PIV visualized experiments and CFD numerical computation
3.1.1 Visualized experimental platform based on PIV

The visualized experimental platform based on PIV is shown in Fig. 15. The equipment is composed of high speed camera, high pressure Xenon lamp, computer, tracing particles and pressure gauge. The labyrinth channel with an area of 1mm² could be observed by a high speed camera and a microscopic len. The camera could be connected with the computer through USB 2.0 interface to analyze and process the measured data of the flow field.

The experimental samples (Fig. 16(c)) were composed of RP parts (the channels) and PMMA plates. The structure of the experimental sample was like a sandwich. Two completely

identical PMMA plates (Fig. 16(a)) and two RP parts (the channel structure can be obtained if correctly placed, like Fig. 16(b)) were connected by ten bolts. The two PMMA plates used as the channel wall were placed at both sides of the RP parts. The flow behavior in the channel could be visualized due to the transparency of the PMMA plates.
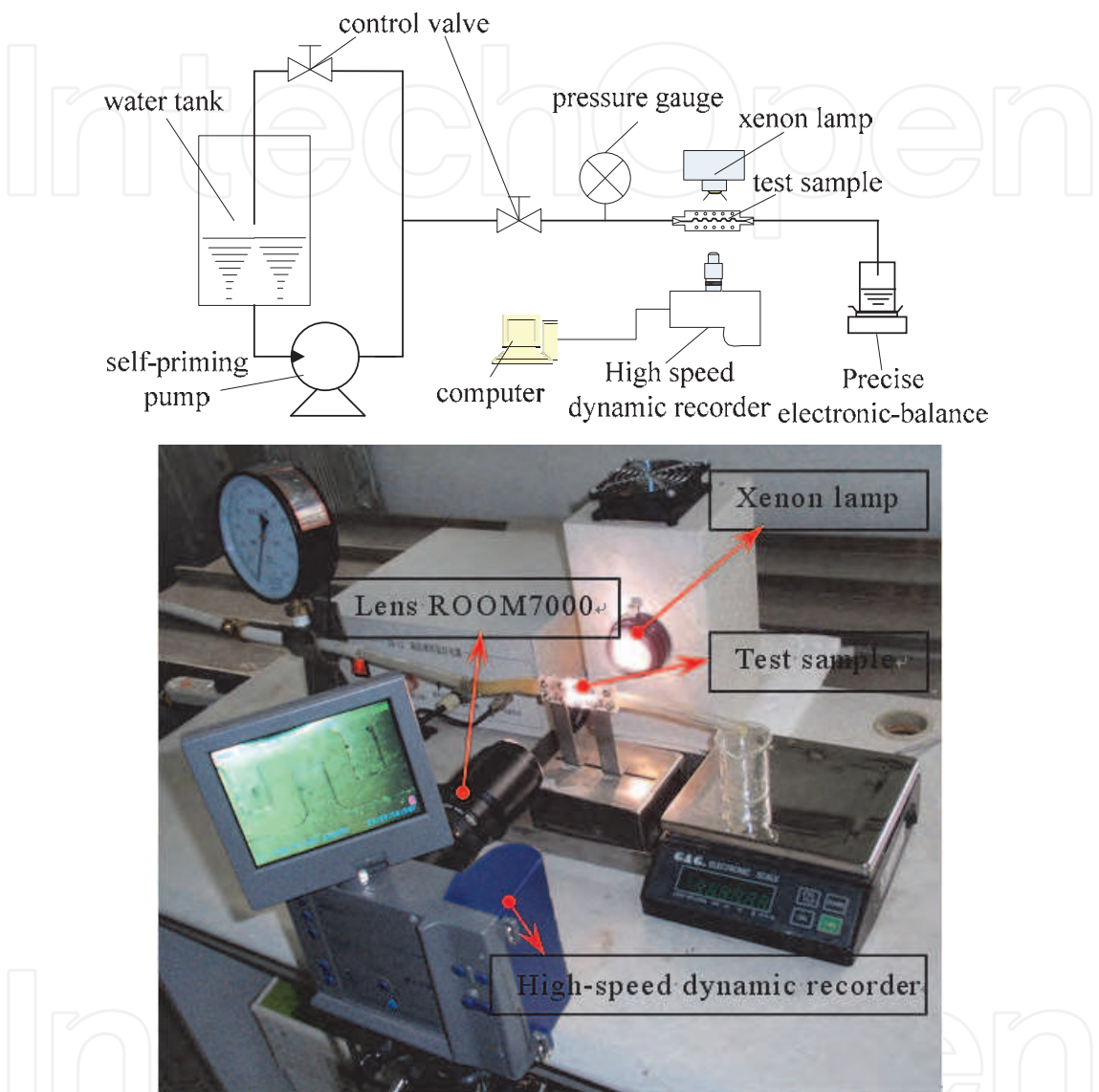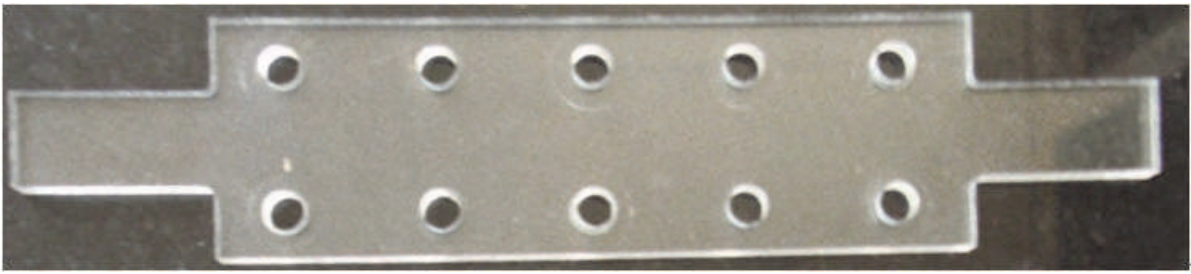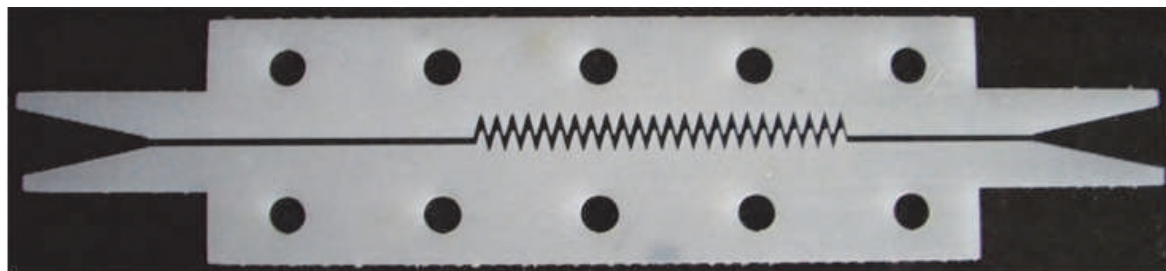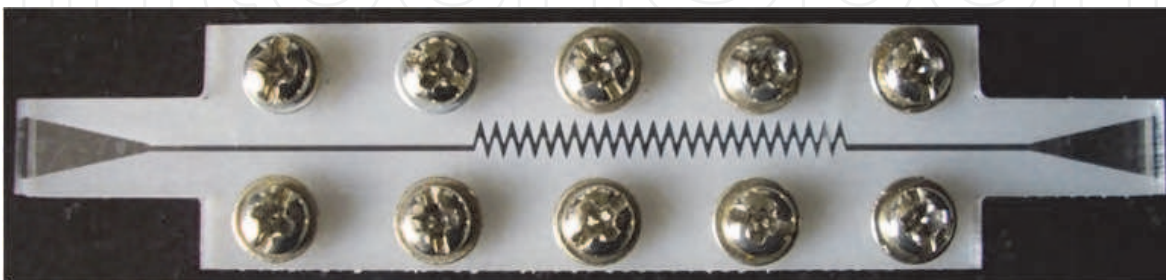

Fig. 15. Scheme of micro-PIV visualized experimental platform

(a) PMMA plate

(b) RP sample

(c) Experimental sample

Fig. 16. Experimental sample and its components

3.1.2 The CFD numerical theory

The width of the channel was generally 0.7~2.0 mm, and the fluid water within the channel was continuous, which met the Navier-Stokes equations and was assumed to be viscous, incompressible and steady at room temperature. The water gravity and surface roughness of the channel wall should be taken into account while the surface tension of the fluid was ignored.

According to the research results of Nishimura (Nishimura et al., 1984a, 1990b), the transition from laminar to turbulent flow occurred when the Reynolds number reached 350 (Kitoh et al., 2005). The channels also had rectangular cross section with a large curvature on the lengthwise section and the Reynolds number was 554~1108 in practical drip irrigation. So the RNG turbulence model and the wall function method were adopted when analyzing the continuous phase water. The equations included mass equation, momentum equation.

The working pressure of the emitter was generally 100KPa, so the inlet boundary condition of the model was chosen to be the pressure-inlet with a pressure P_i=100KPa, and atmospheric pressure of the outlet was used. The discrete governing equations based on the finite volume method were adopted to carry on the numerical simulation and SIMPLE algorithm was also used.

3.2 The analysis of the emitter's hydraulic performance based on single phase

The hydraulic performances of the emitter included macroscopic hydraulic behavior and microscopic hydraulic behavior. The macroscopic hydraulic behavior was mainly indicated by the fluctuation of the flow rate q of the emitter with the water pressure. The microscopic hydraulic behavior was the distribution of the flow field within the labyrinth channels.

Taking the triangle labyrinth channel as an example, the flow behavior in the channel was analyzed. When the inlet pressures were kept at 40KPa and 150KPa, the Reynolds numbers

were 600 and 1300 respectively, which were far below the transition Reynolds number 2300 in smooth straight round pipe. According to the pipeline flow theory, with the centrifugal inertial force, the pressure of the fluid at the lateral was obviously higher than that of the inner in a tortuous flow channel, which would generate vortex and secondary flow more easily. The greater the rotational angle was, the greater the strength , the range of vortex and secondary flow would be, meanwhile the time that the eddy vortex and the secondary flow occur would be advanced, which was beneficial to the earlier appearance of the turbulence (Nishimura et al., 1990; Gerolymos et al., 2002; Humphrey et al., 1981; Arnal et al., 1992; Winoto & Crane, 1980). Fig. 17 shows the flow behavior represented by the streamline in the same flow channel unit at different Reynolds numbers. For the tortuosity of the labyrinth channel was relatively larger, some small circulating vortexes appeared at the sharp corner of the labyrinth channel, but the streamline was still symmetric with the central plane of the channel. With continual rising of the Reynolds number, the inertia force was increasing constantly , which maight generate phase difference between the streamline and the flow channel shape. Meanwhile, the strength and the range of the circulating vortexes were thereby expanding, but the center of them shifted down. When the Reynolds number was 80, the center of the first vortex moved to midway of the channel, which provided the space for the second vortex to occur. Subsequently, the second vortex gradually enlarges, the whole flow state turns to be three-dimensional because of the oscillation and fluctuation of the shear layer.
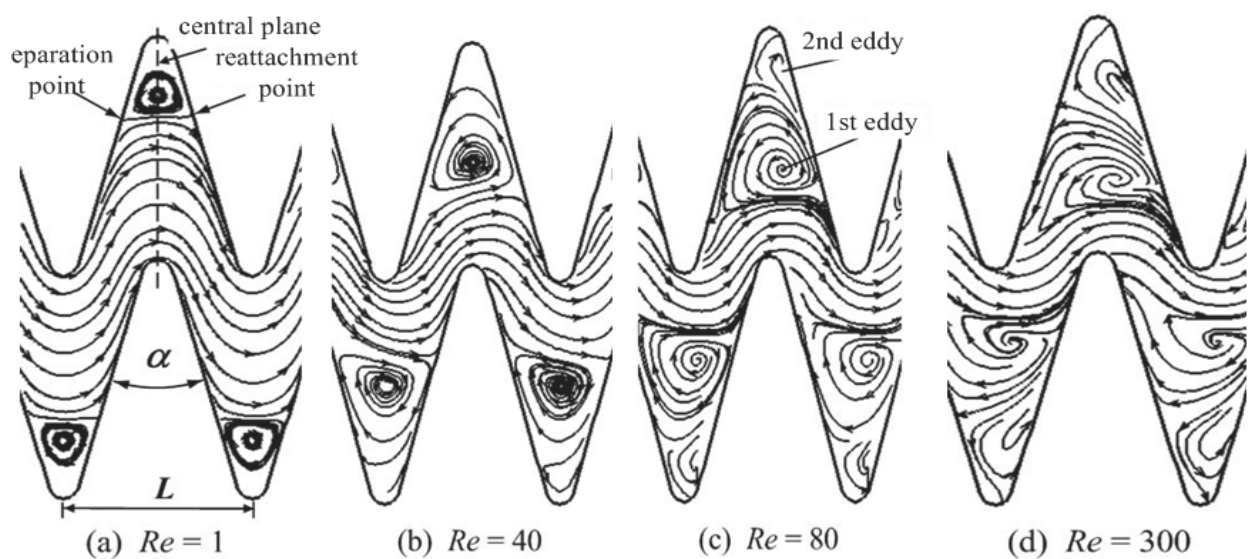

Fig. 17. Distribution of path lines in labyrinth channel element at different Re

Before the fluid in the tortuous channel arrived at the central plane of the rotational angle, the fluid was to be separated because the pressure of the lateral was relatively higher than that of the inner, then the sign of the pressure gradient would reverse so as to favour the reattachment of fluid and wall, which is shown in Fig. 17(a). Fig. 18 shows the distribution rule between the separation point and the reattachment point under different reynolds conditions. The position of the separation point and the reattachment point would be gradually away from the corner of the channel at the initial stage. However, the position of the separation point was little changed and basically stable near the outlet when the Reynolds Number increased grater than 40, the position of the reattachment point wasn't

tended to be stable until the Reynolds Number increased to 100. The change of position at the separation and the reattachment point also indicated that the central position of the vortex in the labyrinth channel successively moved to the bottom-right first and then to the bottom-left with the increasing of the Reynolds Number. While the Reynolds Number increased form 250 to 300, the anomalous change happened to the position of the separation point and the reattachment point. According to the experimental results by Rush et al, the fluid in the channel became unstable as the Reynolds Number went from 250 to 300 (Rush et al., 1999), which was the turning point from laminar flow to turbulent flow. The conclusion showed that the flow were turbulent under the whole working pressure conditions.

Fig. 19 shows the experimental results of the flow rate for two types of emitters in the pressure range 40～150KPa and the predicted values on the basis of two kinds of numerical models. The distribution rule of the curves indicated that the numerical calculation was applicable to predict the flow rate of the emitter to a certain extent.
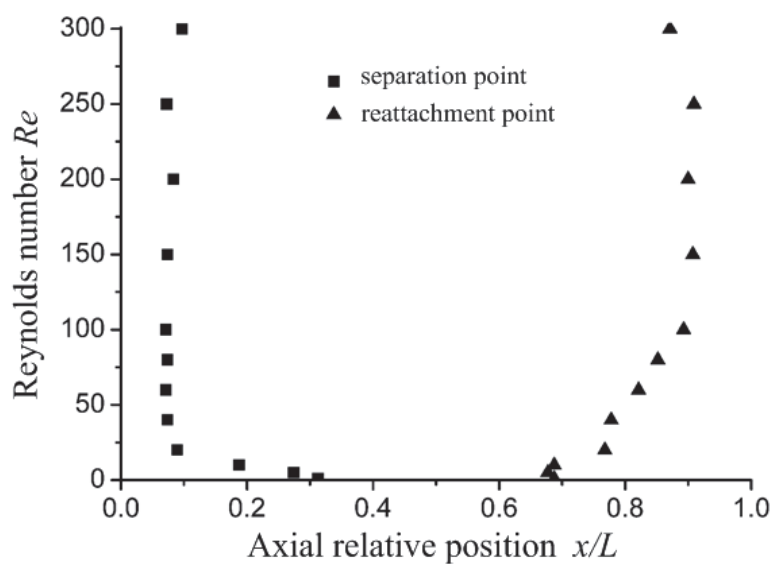
Fig. 18. Distribution of separation points and reattachment points in the labyrinth channel
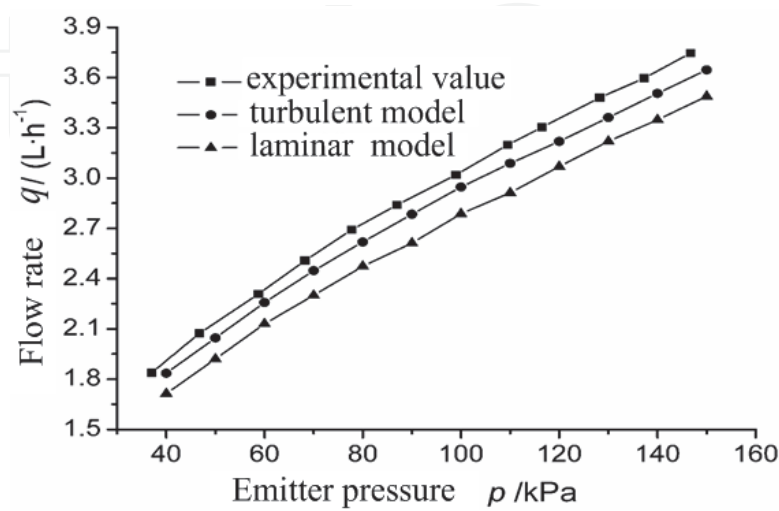
Fig. 19. Distribution of separation points and reattachment points in the labyrinth channel

The pressure and flow rate obtained by using laminar flow model and turbulent flow model were $q_{lam}=0.237p^{0.536}$ and $q_{turb}=0.27p^{0.518}$ respectively. The pressure and flow rate obtained by experiments was $q_{exp}=0.286p^{0.515}$. The average errors by comparing the experimental results with the laminar flow model and the turbulent flow model were 9% and 4% respectively. Based on the above-mentioned results, the numerical prediction showed that the result using the turbulent flow model was more reasonable than that using the laminar flow model.

The distribution of the flow filed was researched by using PIV visualized test bed when Reynolds number was 213. The experimental result is shown in Fig. 20(b), which was post processed by image processing software. Fig. 20(a) shows the simulation results of the flow field. The twelfth channel unit, counting from the emitter's inlet, was selected as the object of comparison and analysis. The length of the arrow represented the magnitude of the velocity. Except for a few sparkles, the main flow zone and low-speed zone were obviously displayed. The numerical results and experimental results were in good agreement.

(a)simulating result   (b)experimental result
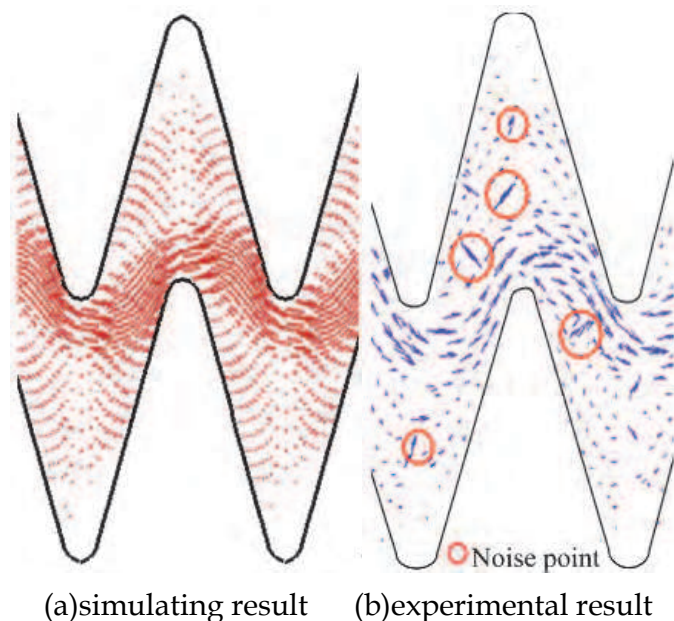
Fig. 20. Velocity vector graph of the flow field when Re=213

For the velocity field was obtained by processing the PIV images, the intuitiveness of the experiment was not obvious. However, the dyeing line method could overcome this shortcoming. Fig. 21 shows the change process of streamline under different Reynolds conditions. The channels in the six figures were composed of three units of the same part in the same test-piece(the twelfth unit from the inlet).

From the above results, we could find that the transition process from laminar flow to turbulent flow in the labyrinth channel was different from that in smooth straight flow channel. For the purpose of improving hydraulic behavior, the turbulent state in labyrinth channel was expected theoretically. From a hydraulic viewpoint, critical Reynolds number was expected to be small. The relationship between the labyrinth-channel structure and Reynolds number was analyzed quantitatively in terms of the distribution features of the separation point and reattachment point, which provided a theoretical basis for the design of the labyrinth-channel structure.
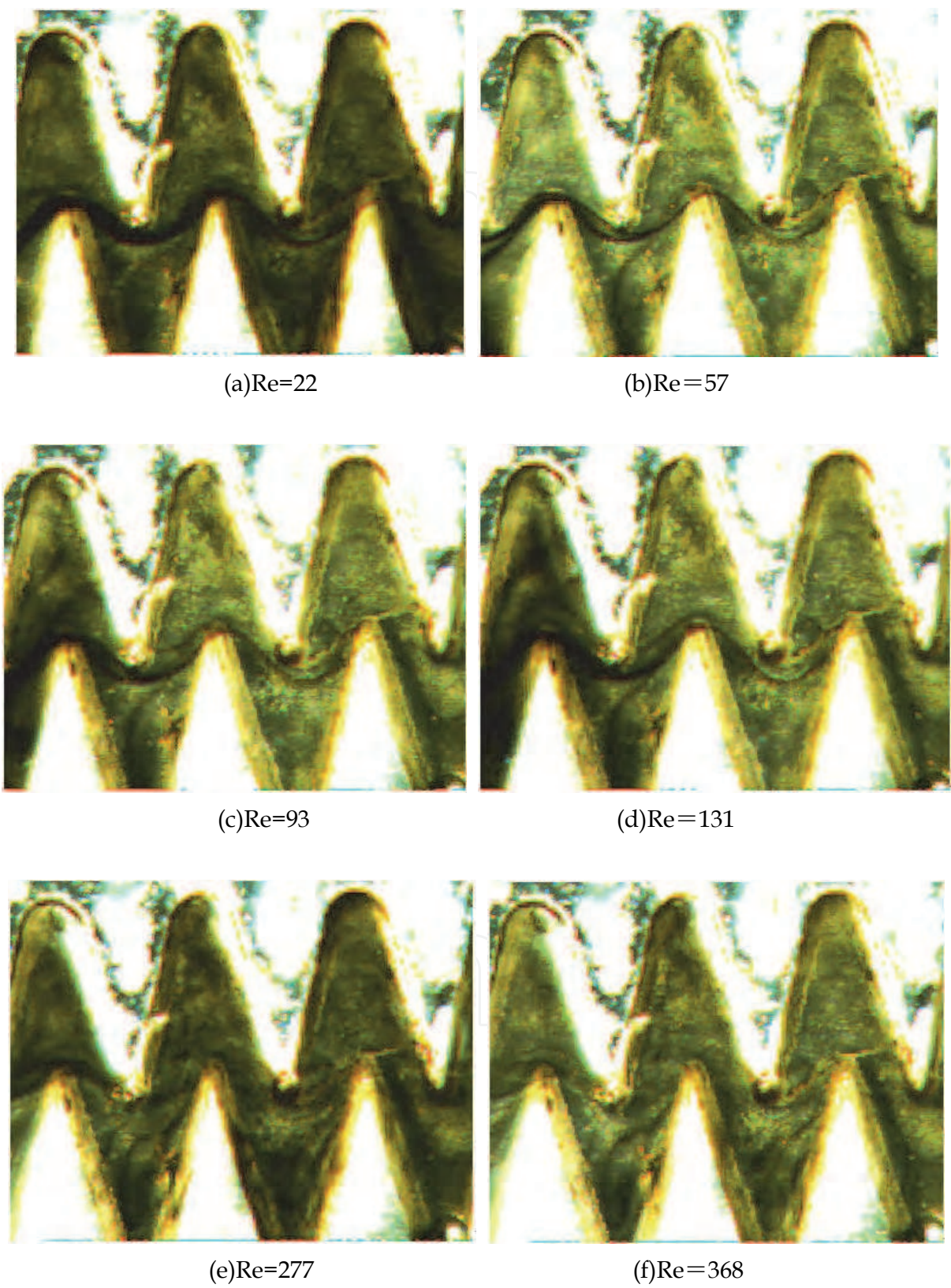
(a)Re=22   (b)Re＝57

(c)Re=93   (d)Re＝131

(e)Re=277   (f)Re＝368

Fig. 21. Flow field displayed via dye experiment

3.3 Research on the particle-wall collision behavior

Some micro particles and microorganism will enter the emitter channel even the irrigation water had been filtered, which might lead to deposition and result in clogging if the particles could not pass through the channel smoothly (Wei Z. et al, 2008; Zhang et al., 2007; Padmakumari & Sivanappan, 1985; Gilbert et al., 1977). In order to analyze the flow state and observe the flow field inside the emitter channel, the CFD (Computational Fluid Dynamics) method was used to conduct numerical simulation of water-sand two phase flow in the micro channel. The flow field distribution of water (continuous phase), and the trajectories of sand (particle phase), were analyzed and the clogging mechanism of micro channel was revealed.

3.3.1 Collision and rebound theory model

In order to establish an accurate numerical model of water-sand two phase flow, it is necessary to observe the trajectories of the particles and the collision between particles and the wall in the channel by experiments before doing numerical simulation.

Experimental results showed that some sands in the water are rebounded to main flow zone after collision with the emitter wall while some others moved slowly along the wall or directly adhered to the channel wall. With the deposition of sand, the emitter was clogged. Particle-wall collision is a main cause of emitter clogging. However, when using computational fluid dynamics software to do the numerical simulation of the labyrinth channel, the key parameters (the collision and rebound coefficient of the particle-wall) are usually set according to experiences rather than determined by the experiments. So the following experiments were used to determine the particle-wall collision and rebound coefficients.

The particle-wall collision was shown in Fig. 22. The rebound coefficient is decomposed to normal coefficient R_{cn} and tangential coefficient R_{ct}. The normal and tangential rebound coefficients respectively reflect the normal and tangential changes of the particles momentum after collision. Where, α is the incident angle and β is the reflect angle.
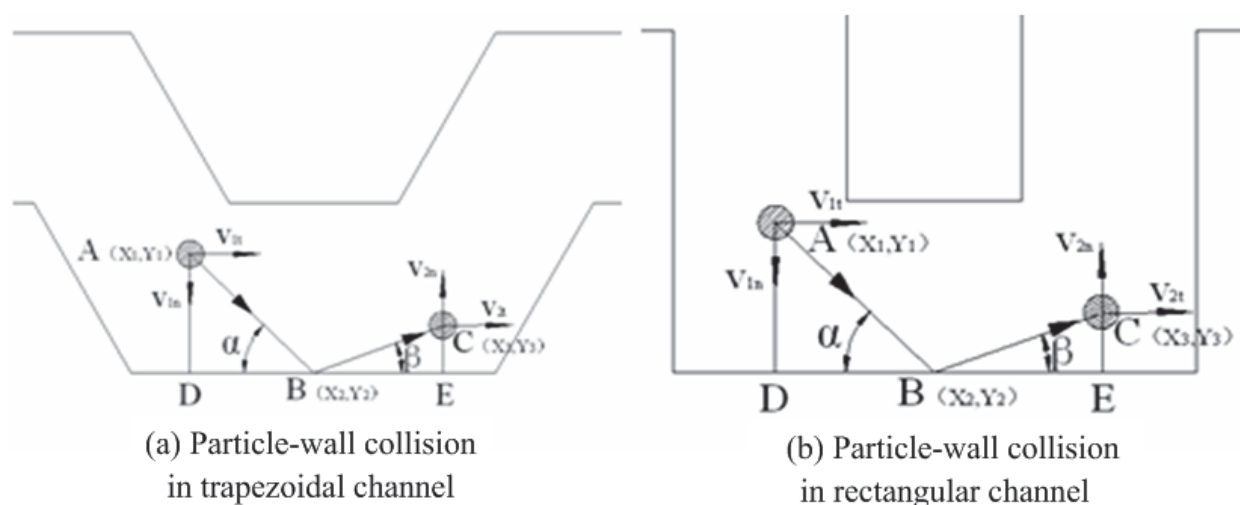

Fig. 22. Collision model between sand and channel's wall

As shown in Fig. 22, the location of the sand was tracked at different times (at times t, t+Δt and t+2Δt). The lines connecting the adjacent points can be approximately taken as the sand

trajectory as the time interval Δt was rather small (0.5ms). Thus the velocity of particle before collision is approximately $V_1 = |AB|/\Delta T$, while after the collision $V_2 = |BC|/\Delta T$. The particle velocity is decomposed tangentially and normally, and the tangential and normal rebound coefficients, incident angle α and reflection angle β were obtained according to the geometric relationship.

From the geometric relationship, it can be obtained:

$$|AB| = \sqrt{(X_2 - X_1)^2 + (Y_2 - Y_1)^2} \tag{1}$$

$$|BC| = \sqrt{(X_3 - X_2)^2 + (Y_3 - Y_2)^2} \tag{2}$$

Decomposing the particle velocity before and after collision, the tangential velocity before collision is:

$$V_{1t} = V_1 \cos\alpha = \frac{|AB|\cos\alpha}{\Delta T} \tag{3}$$

The normal velocity before collision is:

$$V_{1n} = V_1 \sin\alpha = \frac{|AB|\sin\alpha}{\Delta T} \tag{4}$$

The tangential velocity after collision is:

$$V_{2t} = V_2 \cos\beta = \frac{|BC|\cos\beta}{\Delta T} \tag{5}$$

Thus, the normal rebound coefficient is:

$$V_{2n} = V_2 \sin\beta = \frac{|BC|\sin\beta}{\Delta T} \tag{6}$$

Thus, the tangential rebound coefficient is:

$$R_{ct} = \frac{V_{2t}}{V_{1t}} = \frac{|BC|\cos\beta\Delta T}{|AB|\cos\alpha\Delta T} = \frac{\sqrt{(X_3 - X_2)^2 + (Y_3 - Y_2)^2}\cos\beta}{\sqrt{(X_2 - X_1)^2 + (Y_2 - Y_1)^2}\cos\alpha} \tag{7}$$

The normal rebound coefficient is:

$$R_{cn} = \frac{V_{2n}}{V_{1n}} = \frac{|BC|\sin\beta\Delta T}{|AB|\sin\alpha\Delta T} = \frac{\sqrt{(X_3 - X_2)^2 + (Y_3 - Y_2)^2}\sin\beta}{\sqrt{(X_2 - X_1)^2 + (Y_2 - Y_1)^2}\sin\alpha} \tag{8}$$

Where

$$\sin\alpha = \frac{|AD|}{|AB|}, \quad \sin\beta = \frac{|CE|}{|BC|}, \quad \cos\alpha = \frac{|BD|}{|AB|}, \quad \cos\beta = \frac{|BE|}{|BC|} \tag{9}$$

Through these above derivation, we can get the collision and rebound coefficients.

3.3.2 Experimental measurement of particle-wall reflect coefficients

Taking trapezoidal labyrinth channel as the example, it is shown how to measure the rebound coefficient. The experimental sample is shown in Fig. 23 and Fig. 24.
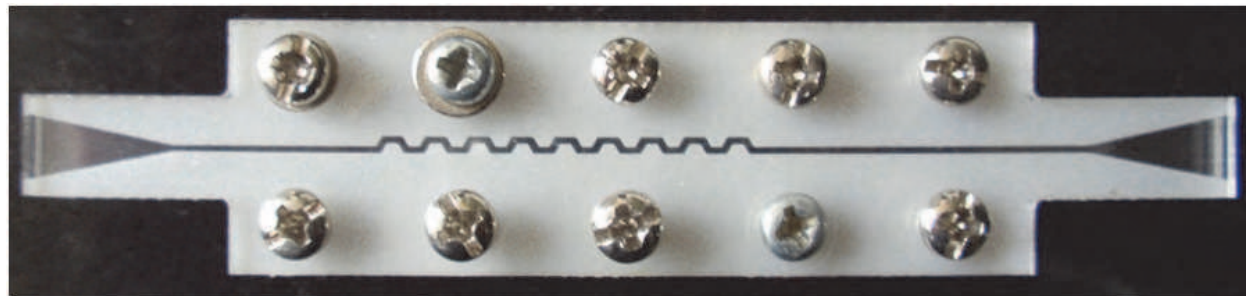

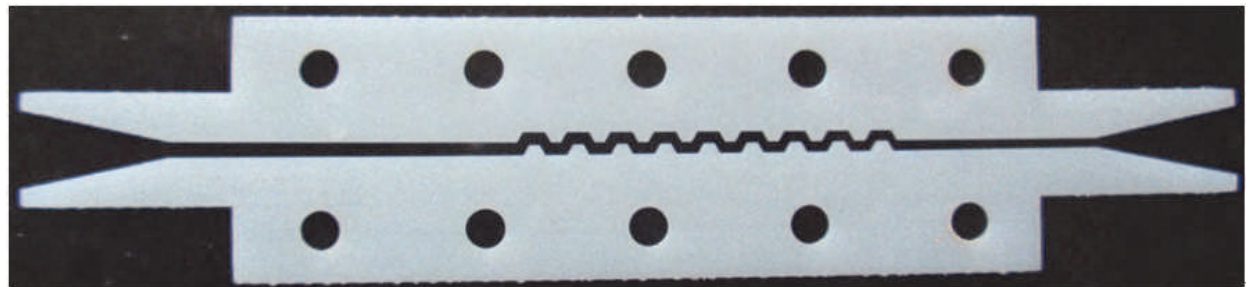Fig. 23. Experimental sample of labyrinth channel

Fig. 24. Experimental sample based on SLA

The collision between sands and emitter wall was observed and recorded by PIV visualized test bed, and then the video segmentation tools were used to pick up all the frames of the video, so the continuous movement images of the sand were obtained. Through processing and analyzing these images based on the computational model of the rebound coefficient, the collision and rebound coefficients in different channels were obtained.

Hydraulic behavior and particle-wall collision of different kinds of labyrinth channel emitters were observed by PIV test bed. The reflect coefficients of 300 grains were measured under the same pressure. The mean value was viewed as the coefficient at this pressure. The relationships between pressure, rebound coefficient and flow rate were shown in Table 5.

Pressure （kPa）	P* （kPa）	R_{ct}	R_{cn}	Q(L/h)
20	0.2857	0.768089	0.363286	3.27
30	0.4285	0.828028	0.440756	4.78
40	0.5714	0.839024	0.465534	5.94
50	0.7142	0.866197	0.350354	6.72
60	0.8514	0.884615	0.258125	7.62
70	1	0.856295	0.327147	8.70

Table 5. The relationship among pressure, rebound coefficient and flow

Curve fitting of pressure and tangential rebound coefficient:

$$R_{ct}=0.7584+0.128P^* \tag{10}$$

Curve fitting of pressure and normal rebound coefficient:

$$R_{ct}=0.4755-0.168P^* \tag{11}$$

P* is the normalized pressure.

Through the above experiments, the rebound coefficient between sand and channel wall can be obtained which can provide theoretical basis for the setting model's boundary conditions for water-sand two phase flow.

3.4 Studying the clogging problem in emitter

The clogging mechanism was studied with SiO_2 being the tracking particles. The tracking particles density was 2320kg/m³ and their average diameter was 67.6μm. The experimental conditions were as follows: the inlet pressure was 100kPa, and the particle density was 500ppm. The flow behavior of the tracking particles was recorded by a high speed shooter (shown in Fig. 25 and 26).

(a) arc labyrinth channel   (b) trapezoidal labyrinth channel
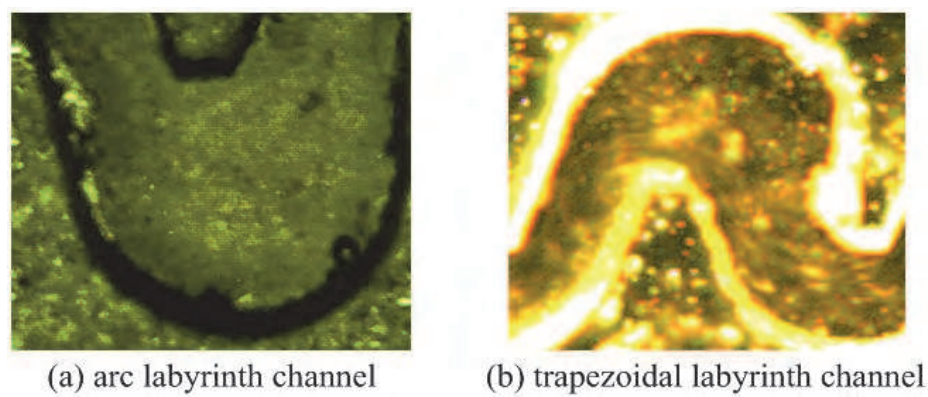
Fig. 25. PIV-graph of the water-sand behaviour

(a) flow behavior displayed   (b) flow behavior displayed
by tracking particles   by dyeing liquor
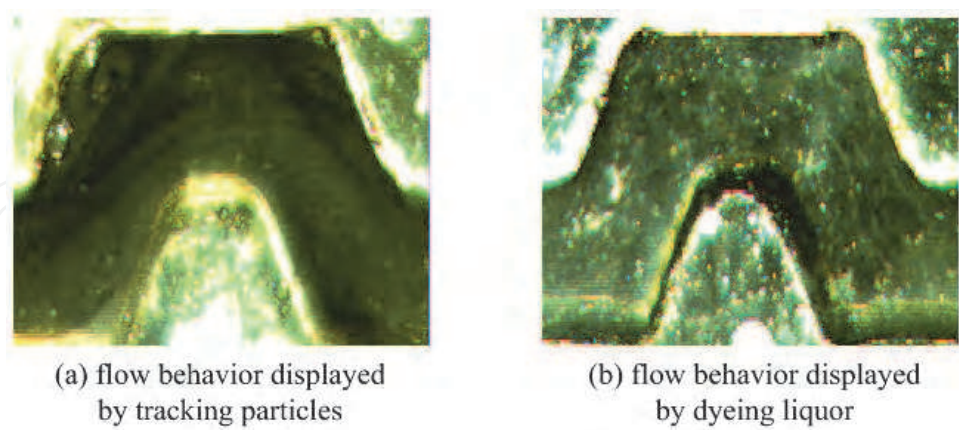
Fig. 26. Flow behavior display

The clogging of the micro-channel is shown in Fig. 27. Sand was deposited at the position that has low flow velocity according to the simulation results. Some conclusions could be obtained: the existence of low velocity regions and the vortex regions is the main reason leading to emitter clogging; and the correctness of the CFD analysis is verified, so the CFD analysis can be used in structural optimization designing of the emitter channel.

(a) starting stage of clogging

(b) developing stage of clogging

Fig. 27. Clogging status when the sand particles are compulsory entered into the channel

Concluding from the simulation and experimental results, the clogging problem can be resolved by removing the low velocity regions and vortex regions. The flow field and the particle moving trajectory in arc labyrinth channel and rectangular labyrinth channel were analyzed, finally, an optimized channel structure was designed. CFD analysis was implemented on the optimized channel and the results are shown in Fig. 28. The low velocity region and vortex region were mostly eliminated in the optimized channel. This labyrinth channel was named as anti-clogging labyrinth channel.

The optimized emitter was fabricated with rapid prototype technique and the anti-clogging test was performed. Fig. 29 shows the emitter channel after a short period anti-clogging test. Comparing the micro PIV test results with CFD simulation, it is found that the stagnation areas were obviously eliminated and hence the anti-clogging behavior of the emitter was improved.

4. Emitter rapid tooling CAE and products finalization

4.1 Emitter's rapid tooling fabrication and accuracy testing

At present, the main process of emitter's product-finalization is as follows: first, the prototype sample is fabricated by SL RP process; then, the hydraulic behavior test on the prototype sample is conducted, the structure of the emitter is determined if the experimental results are satisfying, or it needs to be redesigned and the above processes should be repeated. Since layer superposition (thickness 0.1mm) is the principle of rapid prototyping, step effect is obvious in emitter fabrication which cause roughness on the emitter surface. To

solve this problem, rapid prototyping and CNC wire cutting were introduced into the emitter development process. CNC wire cutting was used to fabricate the emitter's channel. RP was used to fabricate the emitter matrix. Then the emitter matrix and emitter channel were assembled to form the prototype of the sheet-emitter.
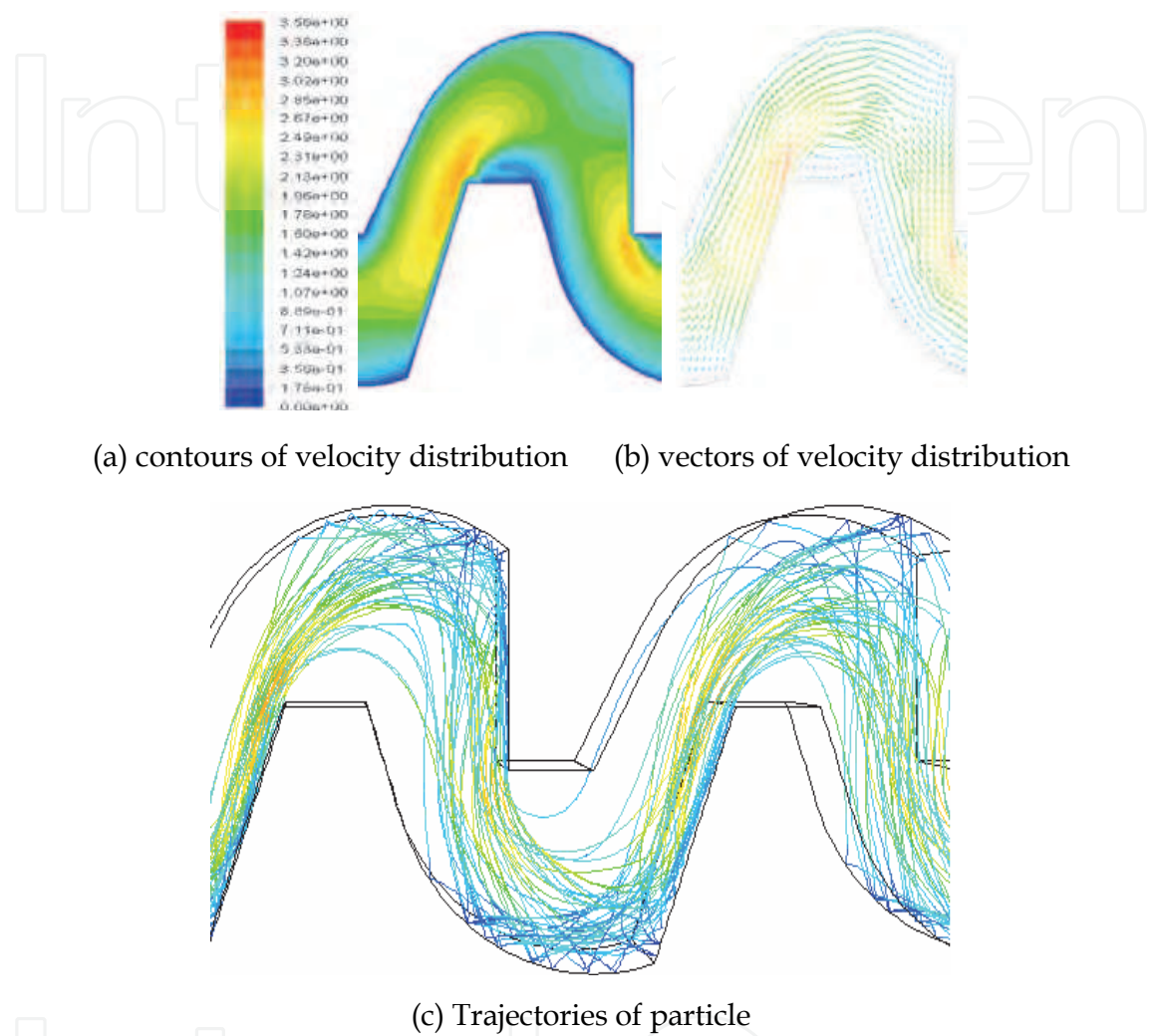

(a) contours of velocity distribution   (b) vectors of velocity distribution

(c) Trajectories of particle

Fig. 28. Analyzing on optimized labyrinth channel

Fig. 29. Clogging status in the optimized emitter

The process of sheet-emitter small batch producing is shown in Fig. 30.
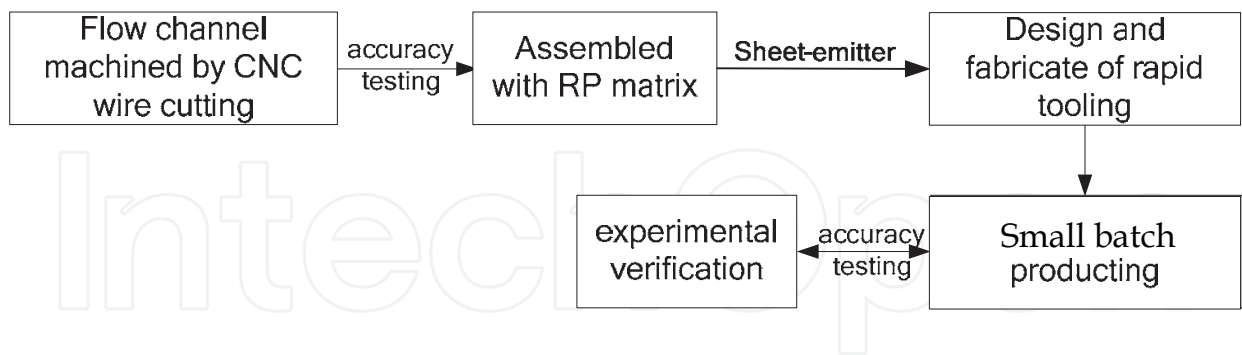
Fig. 30. Manufacturing process of sheet-emitter

When the emitter has small-size channel, the relative size error will be very large which cannot meet the accuracy requirement. In Fig. 31, the width error in certain part of the channel is larger than 5%, and the shape error can reach up to 10%. Those errors will affect the flow behavior, and finally affect the emitter's hydraulic and anti-clogging performance. Under this condition, the hydraulic performance obtained from experiments cannot reflect the actually situation.

(a) The measurement results of RP sample (b) Design size of the channal
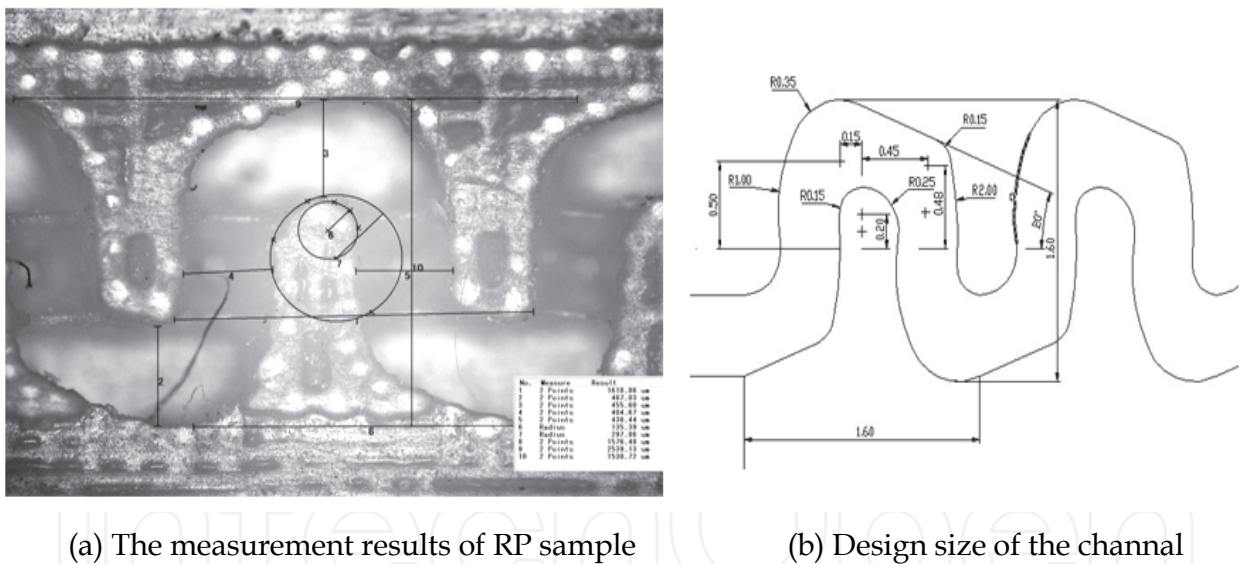
Fig. 31. The channel's RP forming accuracy compared with the designed size

Then the forming accuracy of the channel by CNC wire cutting was analyzed. Accuracy measurement had been made on the cutting channel through microscope. The main dimensions of the channel are arc radius and channel width. The design width of channel was 0.4mm and the arc diameter was 0.17mm. From the measurement results, the range of the size error is from 0.24% to 4.82%, which is less than 5%. Namely, the emitter sample can meet its accuracy requirement.

From the measurement results, it showed that the emitter could meet the accuracy requirements by CNC wire cutting. With the technology of RP (manufacturing complex samples), the matrix of emitter is fabricated which is assembled with channel fabricated by CNC wire cutting. The whole model is shown in Fig. 34.
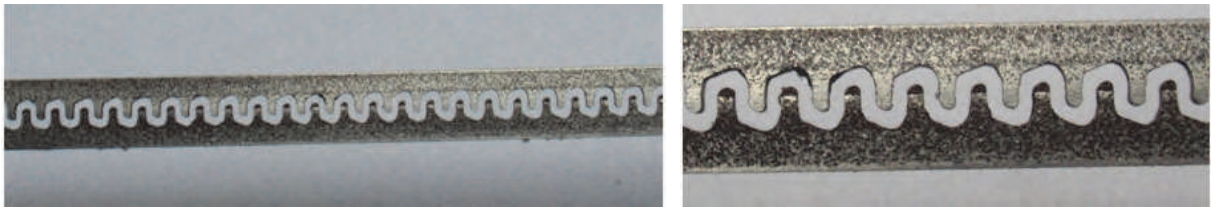
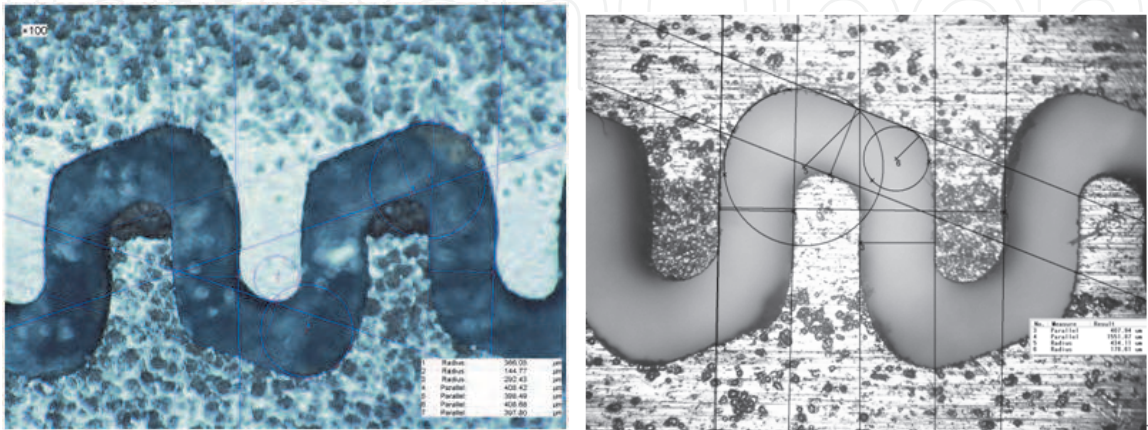Fig. 32. Oblique teeth channel under wire-cutting process

Fig. 33. Accuracy measurement of helical sample under wire-cutting process

Fig. 34. Oblique teeth channel emitter obtained by assembling the wire-cutting samples and the RP sample

Rapid tooling is fabricated using the assembled sample. With the advantages of perfect simulation effect, high strength and low shrinkage rate, the silicon rubber (PDMS) is chosen to produce rapid tooling. As the silicon rubber doesn't react with the material of RP, no wrinkle is produced in the fabrication process and good surface quality can be obtained. The mold fabricating process of silicon rubber is shown in Fig. 35.
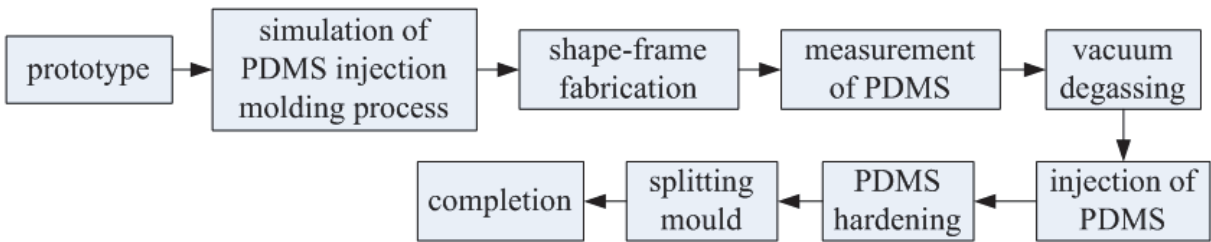
Fig. 35. Manufacturing process flow of PDMS mould

Before RT fabricating, the software MOLDFLOW was used to determine the best process parameters and the injecting position. Then RT mold (Fig. 36) was produced.
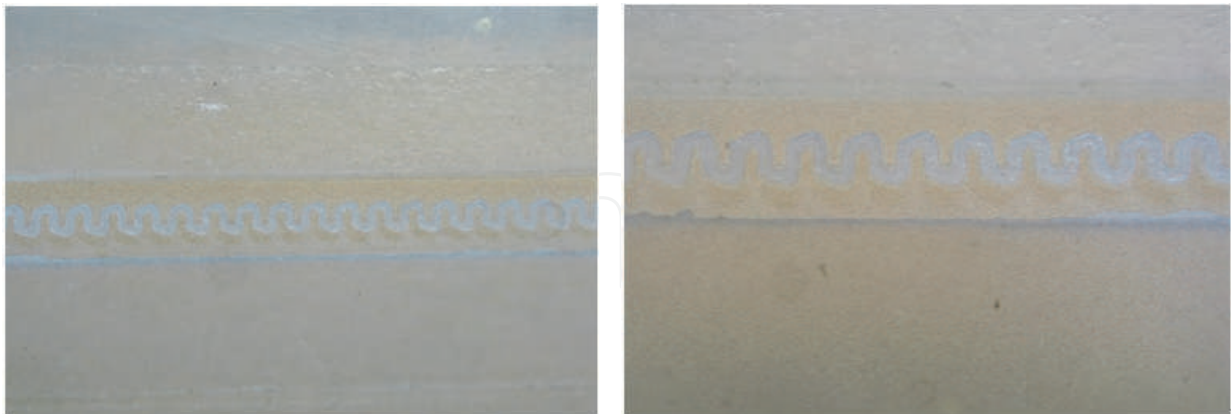
Fig. 36. Silicon rubber mold

Small batch of emitter products were obtained using the silicon rubber mold. One of the products is shown in Fig. 37. Main dimensions of the emitter were measured by a microscope, and the results are shown in Fig. 38. The range of the dimension errors is from 0.23% to 4.82%, less than 5%. This result can meet design accuracy requirement.

Fig. 37. Oblique teeth channel sheet-dropper products in polyurethane
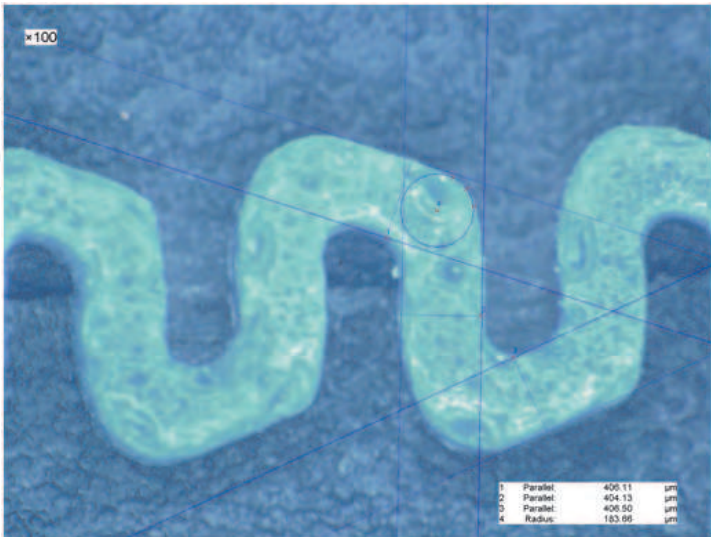
Fig. 38. Dimensions measurement on oblique teeth channel sheet-dropper

Drops were embedded in polyethylene pipe in the practical application. To avoid additional effect on test, outside of emitter was sealed with polyethylene tape to ensure good sealing. After installation, the result is shown in Fig. 39(a). During the hydraulic performance experiment, ink was injected into the upstream relative to the flow in the channel to test the sealing performance. The result was shown in Fig. 39(b), the sealing performance was perfect as little of the ink was appeared at the outer of the channel. Finally, the pressure-flow performance and anti-clogging performance test were conducted on the products.

(a) assembled sample   (b) sealing test results
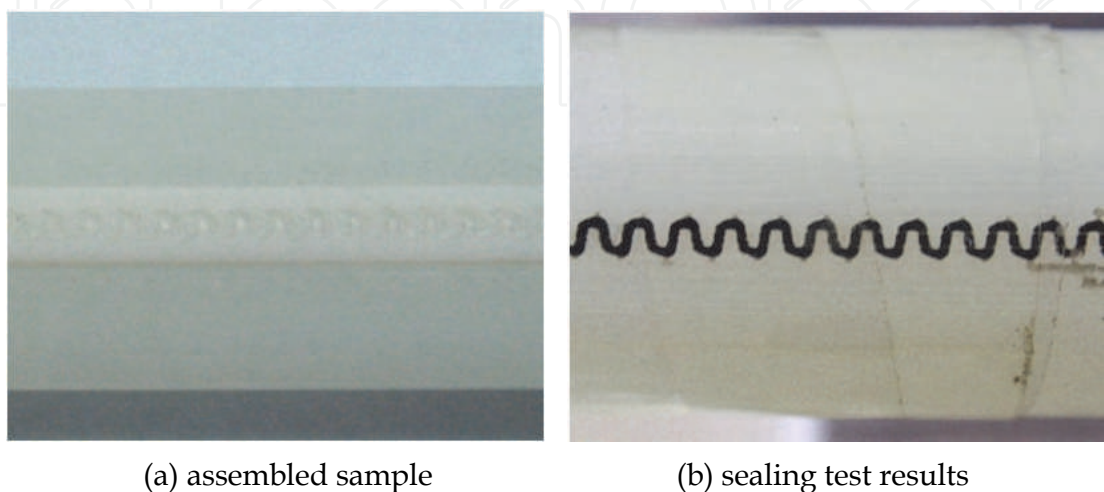
Fig. 39. Oblique teeth channel sheet-dropper's combination and its sealing test

The experimental results and analysis of hydraulic behavior are shown in Fig. 40. Through analyzing the experimental results, the flow rate of oblique-teeth channel sheet-dropper can be obtained: $Q = 0.0961x^{0.5776}$. The flow state index is 0.5776, which indicates that the oblique-teeth channel is insensitive to pressure changes and has excellent hydraulic behavior.
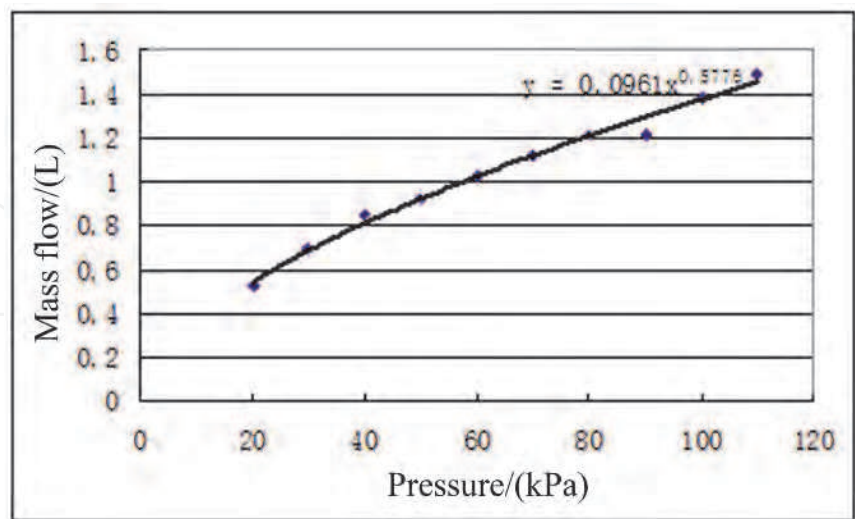

Fig. 40. Hydraulic performance of the oblique-teeth channel sheet-dropper

Then the anti-clogging experiment was conducted. The relationship between emitter's mass flow and time was obtained with inlet pressure being 100kPa. The diameters of tracing particles ranged from F60 to F220. In the experiments, when flow rate was less than,

compared to the initial average flow, 25%, the emitter was considered completely clogged. The anti-clogging experimental results are shown in Fig. 41. The oblique-teeth channel sheet-dropper was not clogged through the eight stages, which meant the emitter had a good anti-clogging performance.
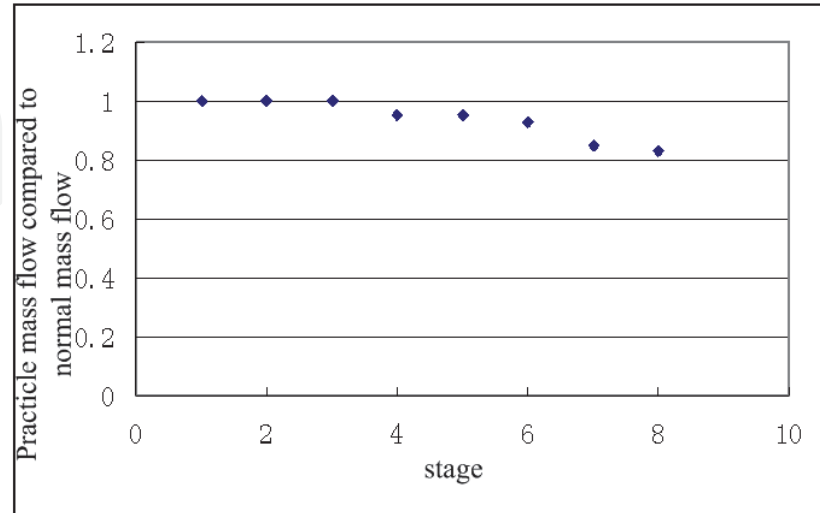

Fig. 41. Anti-clogging performance test on oblique-teeth channel sheet-dropper

With the perfect hydraulic behavior and anti-clogging performance, the test piece could be further applied in development of finalized products.

4.2 Precision emitter fabrication and product finalization

When fabricating labyrinth-channel emitters, EDM could be used to form the cavities of channels. But the fabrication of EDM electrode was very difficult. The discharge gaps would affect mold's accuracy. Therefore, the cavity of flow channel should be fabricated independently by CNC wire cutting as an insert. This method could meet the requirement of "clean-root" and ensure the mold's manufacturing accuracy.
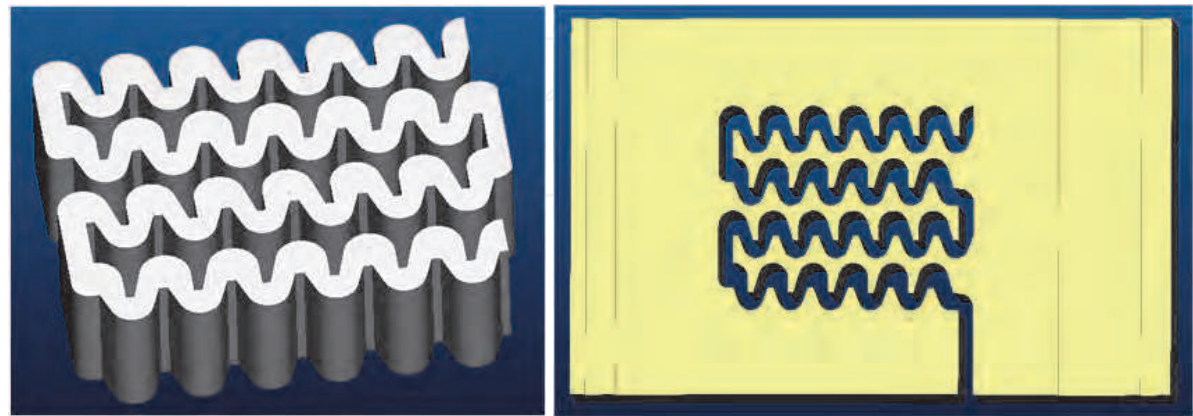

Fig. 42. Diagram of labyrinth grooves and channels inserts pieces

In the calculation of mold's size, the shrinkage of dropper's material should be considered first. The shrinkage of low-density polyethylene was 2.0%. The size of mold cavity was calculated as follows:

$$A_{mold}=(1+s)B_{dropper}\pm\Delta \text{ (tolerance)} \qquad (12)$$

It was difficult to show labyrinth dropper's sophisticated channel structure through two-dimensional design drawing, which was involved in the CAD model of this dripper mold cavity. However, dropper mold's opposite CAD model can be used. Pro/E was used to obtain two-dimensional design drawing from dropper mold's opposite CAD model. The design of the mold cavity (ten cavities in one mold) is shown in Fig. 43.
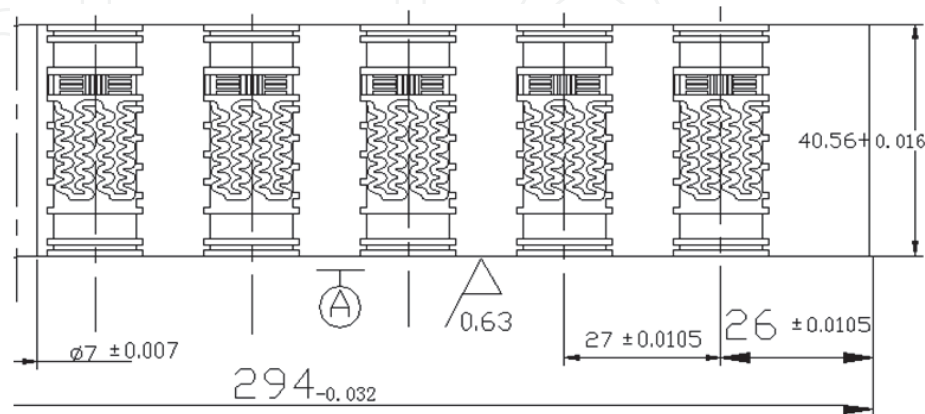

Fig. 43. Mold design of labyrinth channel dropper

In the process of mold design, demoulding convenience should be considered. For the dropper's complex surface and the accuracy requirement, a small core-pulling stroke has to be used to the mold that has a larger molding area, a shallow lateral allowing for the ease of demoulding was adopted in the dropper's demolding process. The outboard cooling scheme was used for the cooling of the mold. Dropper mold assembly is shown in Fig. 44. The structure of the cavity-insert dropper is shown in Fig. 45.
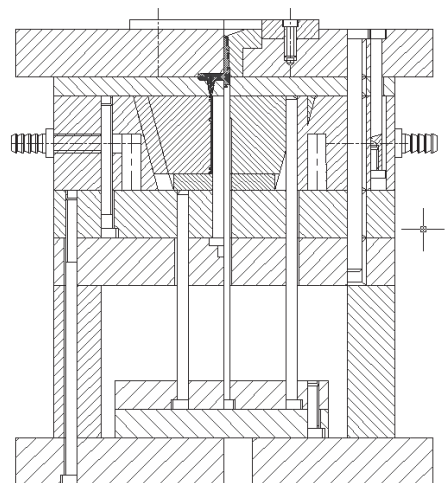The steel mold and labyrinth dropper products are shown in Fig. 46(a) and (b).

Fig. 44. Dropper mold assembly drawings

Using precision mold manufacturing technology could prevent the existence of dead flow. It also ensured the structure has anti-clogging behavior and high manufacturing accuracy.
Insert-embedded dropper with pressure compensating was fabricated based on precision mold manufacturing technology. Mold cavity design was integrated with flow channel and
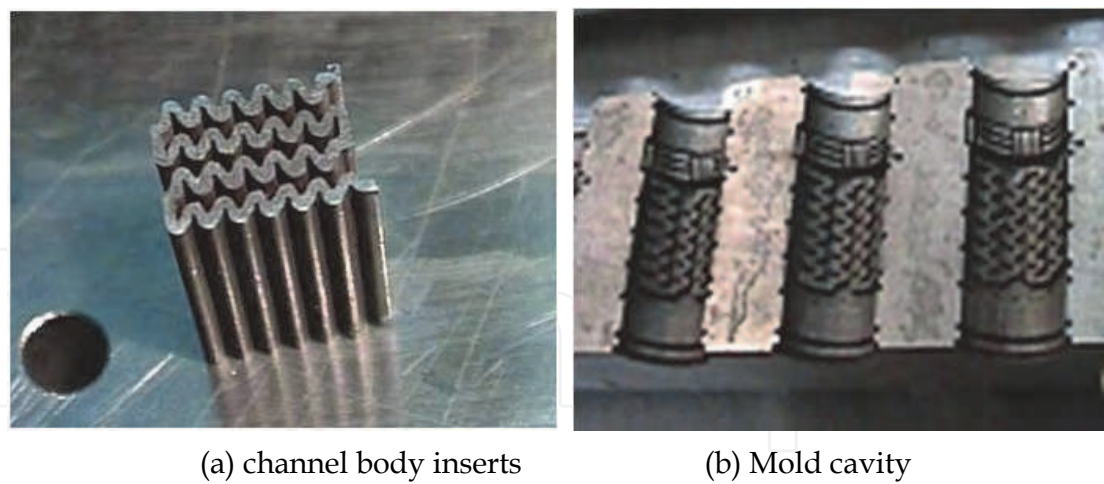
(a) channel body inserts   (b) Mold cavity

Fig. 45. Insert cavity mold structure of the dropper

(a) The overall figure of steel mold   (b) labyrinth dropper Products

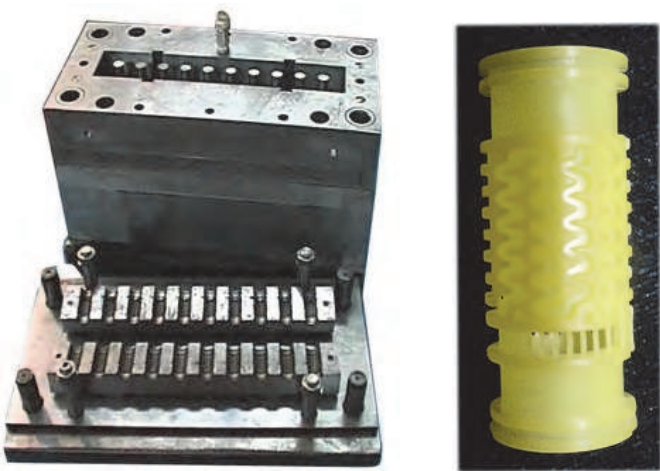Fig. 46. Steel injection mold

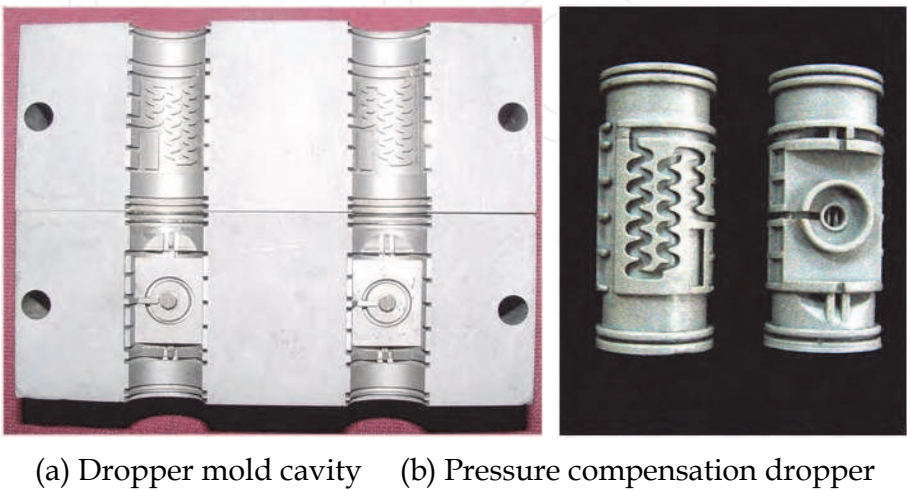(a) Dropper mold cavity   (b) Pressure compensation dropper

Fig. 47. Pressure compensated labyrinth dropper mold

inlet grid. The mold cavity is shown in Fig. 47 (a). Pressure regulators were manufactured separately, and then inserted into cavity. On the injection molding machine, pressure compensating dropper can be obtained which is shown in Fig. 47 (b). And two kinds of molds had been developed as shown in Fig. 48.

Through calculations and experiments, the pressure fluctuation of our products is less than 2%; flow rate is 3.956L/h; flow fluctuation coefficient is 4.26%, which comply with the standard of the National Quality and Technical Supervision Bureau.
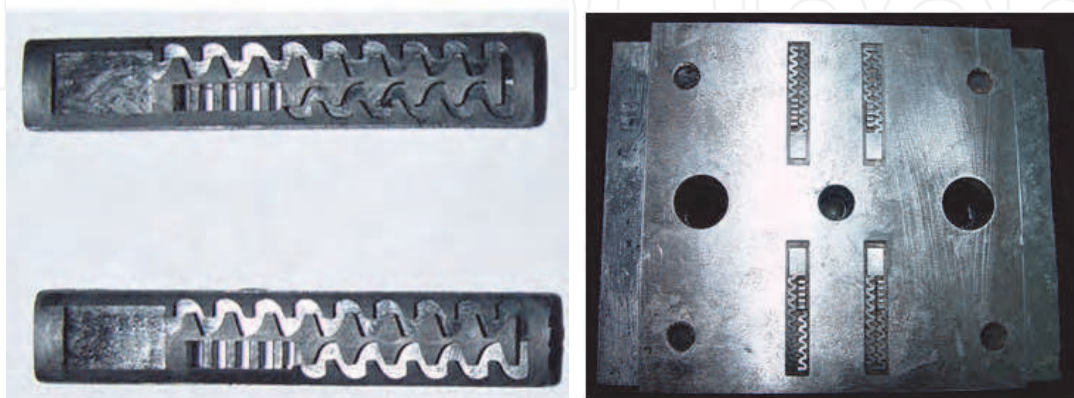
(a) Anti-clogging sheet-dropper   (b) diagram of sheet-dropper's mold

Fig. 48. Anti-clogging sheet-dropper's mold

5. References

Bralts& Vincent, F. (1985). Micro Computer Aided Design of Drip/Trickle Irrigation Submain Units, In: *Drip/Trickle Irrigation in Action, Proceedings of the Third International Drip/Trickle Irrigation Congress,* pp. 452-458, ISBN 091-6150-73-9 Silver Spring, MD, USA. November, 1985

Thompson, T.; Pang, H. & Li Y. (2009). The Potential Contribution of Subsurface Drip Irrigation to Water-Saving Agriculture in the Western USA. *Agricultural Sciences in China* Vol. 8, No.7,(July 2009), pp. 850-854, ISSN 1671-2927.

Lamm F. R.&Camp C. R. (2007). Subsurface drip irrigation, In:*Developments in Agricultural Engineering,* J. E. A. Freddie R. Lamm, S. N. Francis, (Eds). pp. 473- 551, Elsevier, ISBN 978-0-444-50607-8, Oxford, UK

Onder, S.; Caliskan, M. E.; Onder, D.&Caliskan, S.(2005). Different irrigation methods and water stress effects on potato yield and yield components. *Agricultural Water Management,* Vol.73, No.1 (April 2005), pp. 73-86, ISSN 0378-3774

Schwankl L. J. & Hanson L. R. (2007). Surface drip irrigation, In: *Developments in Agricultural Engineering,* J. E. A. Freddie R. Lamm, S. N. Francis, (Eds). pp. 431-472, Elsevier, ISBN 978-0-444-50607-8, Oxford, UK

Cetin O. & Bilgel L.(2002).Effects of different irrigation methods on shedding and yield of cotton. *Agricultural Water Management* Vol.54, No.1 (March 2002) pp. 1-15, ISSN 0378-3774

Wei Z.; Tang Y.; Zhao W. & Lu B.(2007). Rapid structural design of drip irrigation emitters based on RP technology. *Rapid Prototyping Journal* Vol.13, No.5 (2007), pp. 268-275, ISSN 1355-2546

Li Y.; Li G.; Qiu X. & Wang J.(2005). Modeling of hydraulic characteristics through labyrinth emitter in drip irrigation using computational fluid dynamics. *Nongye Gongcheng Xuebao/Transactions of the Chinese Society of Agricultural Engineering* Vol.21, No.3, (March 2005), pp. 12-15, ISSN 1002-6819

Li Y. *et al.*(2008). CFD and digital particle tracking to assess flow characteristics in the labyrinth flow path of a drip irrigation emitter. *Irrigation Science* Vol.26, No.5 (March 2008), pp. 427-438, ISSN 0342-7188

Wei Z.; Tang Y. & Lu B.(2003). A Rapid Manufacturing Method for Water-Saving Emitters for Crop Irrigation Based on Rapid Prototyping and Manufacturing. *The International Journal of Advanced Manufacturing Technology* Vol.21, No.9 (June 2003), pp. 644-648, ISSN 0268-3768

Wei Z.; Tan Y. g; Zhao W. & Lu B.(2005). Structure and hydraulic performance experimental research on labyrinth channels of drip irrigation emitters. *Nongye Jixie Xuebao/Transactions of the Chinese Society of Agricultural Machinery* Vol.36, No.12(December 2005), pp. 51-55, ISSN 1000-1298

Wei Z.; Tang Y.; Wen J. & Lu B.(2008). Two-phase flow analysis and experimental investigation of micro-PIV and anti-clogging for micro-channels of emitter. *Nongye Gongcheng Xuebao/Transactions of the Chinese Society of Agricultural Engineering* Vol.24, No6. (June 2008), pp. 1 -9, ISSN 1000-1298

White D. (2001). Rapid tooling technology, In: *Encyclopedia of Materials: Science and Technology,* K. H. J. Buschow *et al.* (Eds.), pp. 8003-8009, Elsevier, ISBN 978-0-08-043152-9, Oxford, UK

Hosni Y. & Sundaram R.(1996). Rapid Prototyping and Tooling: A survey and Applications in *Current Advances in Mechanical Design and Production VI,* E. E. Mohamed, S. W. Professor Abdalla, A. S. Wifi, Prof (Eds). pp. 511-520, Pergamon, Elsevier Science Inc.ISBN 0-08-042140-7, NY, US

Yan X. & Gu P.(1996). A review of rapid prototyping technologies and systems. *Computer-Aided Design* Vol.28, No.4 (April 1996), pp. 307-318, ISSN 0010-4485

Pham D. T. & Gault R. S.(1998). A comparison of rapid prototyping technologies. *International Journal of Machine Tools and Manufacture* Vol.38, No.10-11, (October 1998), pp.1257-1287, ISSN 0890-6955.

Choi S. H.& S. Samavedam (2002) .Modelling and optimisation of Rapid Prototyping. *Computers in Industry,* Vol.47, No.1,(January 2002), pp. 39-45, ISSN 0166-3615.

Wei Z.; Tang Y.; Cheng Y. & Lu B.(2008). New method for rapid design of the integral pressure-compensating emitters. *Zhongguo Jixie Gongcheng/China Mechanical Engineering* Vol.19, No.12, (June 2008), pp. 1387-1392, ISSN 1004-132X

Zhang J.; Zhao W.; Tang Y. & Lu B.(2010). Anti-clogging performance evaluation and parameterized design of emitters with labyrinth channels. *Computers and Electronics in Agriculture,* Vol.74, No1, (October 2010), pp.59-65, ISSN 0168-1699

Liu H.-s. *et al.*(2010) Flow characteristics in energy dissipation units of labyrinth path in the drip irrigation emitters with DPIV technology. *Journal of Hydrodynamics, Ser. B* Vol.22, No.1 (February 2010), pp. 137-145, ISSN 1001-6058

Li G. Y.; Wang J. D.; Alam M. & Zhao Y. F.(2006) Influence of geometrical parameters of labyrinth flow path of drip emitters on hydraulic and anti-clogging performance. *Transactions of the ASABE* Vol.49, No.3, (April 2006), pp. 637-643, ISSN 0001-2351.

Zhang J.; Zhao W.; Wei Z.; Tang Y. & Lu B.(2007). Numerical and experimental study on hydraulic performance of emitters with arc labyrinth channels. *Computers and Electronics in Agriculture,* Vol.56, No.2 (April 2007), pp.120-129, ISSN 0168-1699

Meng G.; Zhang M.; Zhao W. & Lu Y. (2004). Numerical flow simulation and optimum channel design of drip irrigation emitter. *Hsi-An Chiao Tung Ta Hsueh/Journal of Xi'an Jiaotong University* Vol.38, No.9 (September 2004), pp. 920-924, ISSN 0253-987X.

Wei Z.; Wen J.; Tang Y. & Lu B.(2008). Structural design and rapid development platform of emitters under lower water pressure. *Nongye Jixie Xuebao/Transactions of the Chinese Society of Agricultural Machinery,* Vol.39, No.10 (October 2008), pp. 59-64, ISSN 1000-1298

Wei Q.; Shi Y.; Dong W.; Lu G.& Huang S.(2006). Study on hydraulic performance of drip emitters by computational fluid dynamics. *Agricultural Water Management* Vol.84, No.1-2, (July 2006), pp. 130-136, ISSN 0378-3774

Nishimura T.; Ohori Y. & Kawamura Y.(1984). Flow Characteristic In A Channel With Symmetric Wavy Wall For Steady Flow. *Journal of Chemical Engineering of Japan* Vol.17, No. 5 (March 1984), pp.466-471, ISSN 0021-9592.

Nishimura T.; Murakami S.; Arakawa S.& Kawamura Y. (1990). Flow observations and mass transfer characteristics in symmetrical wavy-walled channels at moderate Reynolds numbers for steady flow. *International Journal of Heat and Mass Transfer* Vol.33, No.5(May 2009), pp. 835-845, ISSN 0017-9310.

Kitoh O.; Nakabyashi K. & Nishimura F.(2005). Experimental study on mean velocity and turbulence characteristics of plane Couette flow: low-Reynolds-number effects and large longitudinal vortical structure. *Journal of Fluid Mechanics* Vol.539, No.00 (September, 2005), pp. 199-227, ISSN 0022-1120

Gerolymos G. A.; Neubauer J.; Sharma V. C. & Vallet I.(2002). Improved prediction of turbomachinery flows using near-wall reynolds-stress model. *Journal of Turbomachinery* Vol.124, No.1(January 2002), pp. 86-99, ISSN 0889-504X

Humphrey J. A. C.; Whitelaw J. H. & Yee G.(1981). Turbulent flow in a square duct with strong curvature. *Journal of Fluid Mechanics* Vol.103, No.00 (February 1981), pp. 443-463, ISSN 0022-1120

Arnal M. P.; Goering D. J. & Humphrey J. A. C.(1992). Unsteady laminar flow developing in a curved duct. *International Journal of Heat and Fluid Flow* Vol.13, No.4, (December 1992), pp. 347-357, ISSN 0142-727X.

Winoto S. H. & Crane R. I. (1980) Vortex structure in laminar boundary layers on a concave wall. *International Journal of Heat and Fluid Flow* Vol.2, No.4, (December 1980), pp. 221-231, ISSN 0142-727X.

Rush T. A.; Newell T. A. & Jacobi A. M.(1999). An experimental study of flow and heat transfer in sinusoidal wavy passages. *International Journal of Heat and Mass Transfer* Vol.42, No.9 (May, 1999), pp. 1541-1553, ISSN 0017-9310.

Zhang J.; Wei G.; Zhao W.; Wei Z. & Lu B.(2007). Numerical analysis on liquid-solid two-phase flows in arc-type channel of the emitter. *Zhongguo Jixie Gongcheng/China Mechanical Engineering* Vol.18, No.5 (March 2007), pp. 589-593, ISSN 1004-132X

Padmakumari O. & Sivanappan R. K.(1985). Sudy of Clogging of Emitters In Drip Systems. In: *Drip/Trickle Irrigation in Action, Proceedings of the Third International Drip/Trickle Irrigation Congress,* pp. 80-86, ISBN 091-6150-73-9 Silver Spring, MD, USA. November, 1985.

Gilbert R. G.; Nakayama F. S. & Bucks D. A.(1977). Trickle Irrigation: Prevention Of Clogging. *Transactions of the ASAE* Vol.22, No.3, (June 1979), pp. 514-519, ISSN 0001-2351
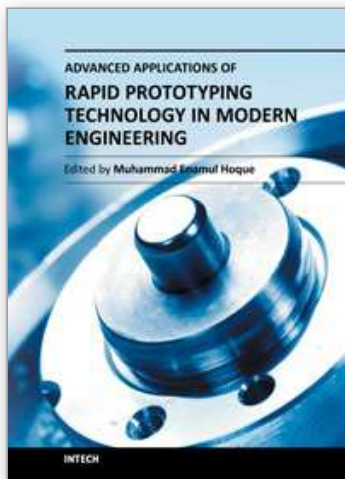
Advanced Applications of Rapid Prototyping Technology in Modern Engineering

Edited by Dr. M. Hoque

Rapid prototyping (RP) technology has been widely known and appreciated due to its flexible and customized manufacturing capabilities. The widely studied RP techniques include stereolithography apparatus (SLA), selective laser sintering (SLS), three-dimensional printing (3DP), fused deposition modeling (FDM), 3D plotting, solid ground curing (SGC), multiphase jet solidification (MJS), laminated object manufacturing (LOM). Different techniques are associated with different materials and/or processing principles and thus are devoted to specific applications. RP technology has no longer been only for prototype building rather has been extended for real industrial manufacturing solutions. Today, the RP technology has contributed to almost all engineering areas that include mechanical, materials, industrial, aerospace, electrical and most recently biomedical engineering. This book aims to present the advanced development of RP technologies in various engineering areas as the solutions to the real world engineering problems.

How to reference

In order to correctly reference this scholarly work, feel free to copy and paste the following:

INTECH
open science | open minds